Evaporation and deposition in porous media

P. Sanaei† [1], C. J. W. Breward [2], M. A. Ellis [2], S. Han [3], B. Holzer [4] H. Ji [5], H. El Kahza [6], S. G. Llewellyn Smith [7], S. Parsa [8], H. Reynolds [2], J. Troy [6], T. Witelski [9], N. Zhang [10], M. Zyskin [2]

[1] *New York Institute of Technology, New York, USA*
[2] *University of Oxford, Oxford UK*
[3] *University of Michigain, Ann Arbor, USA*
[4] *San Diego State University, San Diego, USA*
[5] *North Carolina State University, Raleigh, USA*
[6] *University of Delaware, Newark DE, USA*
[7] *University of California San Diego, San Diego, USA*
[8] *Rochester Institute of Technology, Rochester, USA*
[9] *Duke Univserity, Durham, USA*
[10] *Oregon State University, Corvallis, USA*

(*Communicated to* MIIR *on 15 October 2021*)

Study Group: 37th Annual Workshop on Mathematical Problems in Industry, 14–18 June 2021, University of Vermont.

Communicated by: Taras I. Lakoba, University of Vermont

Industrial Partner: W. L. Gore and Associates

Presenter: U. Beuscher, V. Venkateshwaran, Z. He.

Team Members: C. Breward, University of Oxford, Oxford UK; P. Broadbridge, La Trobe University, Melbourne AU; L. Cummings, New Jersey Institute of Technology, Newark, NJ, USA; D. Edwards University of Delaware, Newark DE, USA; H. El Kahza, New York Institute of Technology, New York, USA; M. A. Ellis, University of Oxford, Oxford UK; S. Han, University of Michigan, Ann Arbor, USA; B. Holzer, San Diego State University, San Diego, USA; H. Ji, North Carolina State University, Raleigh, USA; S. Llewellyn Smith, University of California San Diego, San Diego, USA; K. Naghibzadeh, Carnegie Mellon University, Pittsburg, USA; S. Parsa, Rochester Institute of Technology, Rochester, USA; C. Please, University of Oxford, Oxford UK; H. Reynolds, University of Oxford, Oxford UK; P. Sanaei, New York Institute of Technology, New York, USA; D. Schwendeman, Rensselaer Polytechnic Institute, Troy, New York, USA; J. Troy, University of Delaware, Newark DE, USA; T. Witelski, Duke Univserity, Durham, USA; N. Zhang, Oregon State University, Corvallis, USA; and M. Zyskin, University of Oxford, Oxford UK;

Industrial Sector: Materials processing

Tools: Partial differential equations, free boundary problems, fluid dynamics, reaction-diffusion models, homogenization theory, network models.

† Corresponding Author: ps468@njit.edu

Key Words: Filtration, evaporation, particle deposition

MSC2020 Codes: 74F25, 76Sxx, 76T20, 76M50

Summary

W.L. Gore & Associates, which is a materials science company focused on discovery and product innovation, presented a problem on evaporation and deposition in porous media during the 37th Annual Workshop on Mathematical Problems in Industry (MPI) on June 14-18, 2021. Dr. Uwe Beuscher, who is the lead for the Modeling and Simulation team at W.L. Gore & Associates and his team including Drs. Vasudevan Venkateshwaran and Zhenyu He were the representatives of W.L. Gore & Associates during the MPI 2021 workshop. A team of graduate students, postdoctoral scholars as well as faculties from all around the world, divided in 5 groups and worked on this proposed problem. The first group considered the microscale problem of deposition of solute particles within a single representative pore channel left as the residue from the evaporation of a volatile fluid solution. Their interest was understanding the forms of contaminant particle distributions on the walls of the pore that can occur and how they can potentially lead to clogging of the porous material under repeated use. The motion of a droplet within a pore with sloped sides, where particles are present, was studied by the second group. The third group attempted to discover a homogenization approach to systematically examine averaging the precipitation of particles onto the microscale porous structure and coupling this with the macroscopic motion of the evaporating interface. The fourth group turned the attention to considering a whole porous medium rather than individual pores. They presented a simple mathematical model to describe the key elements of evaporation in porous media, which includes an advection-diffusion equation for the particle transport and deposition of particles within the porous membrane as well as variations in the membrane porosity due to particle deposition and evaporation. Finally, a simplified network model, which provides a viable alternative to a full numerical solution of the dynamics of two-phase flow in evaporation, was studied by the fifth group.

1 Introduction

Evaporation from porous media plays a significant role in many environmental and engineering processes as well as industrial applications [1]. It is a key process affecting land-atmosphere exchanges, surface energy balance and many other biological and engineering applications [28]. Therefore, understanding contaminant transport and deposition patterns during evaporation from porous media is an important factor in many engineering, hydrological and industrial processes [29]. Researchers have looked into this phenomenon

from different perspectives includingthe effects of the solvents properties, the porous internal structure geometry and wettability on the evaporation process as well as stages related to internal transport mechanisms that affect evaporation flux [21, 32, 14, 17].

In certain liquid filtration problems, a fluid flows through a porous media designed to trap solute molecules. In the case under consideration, the porous media is polytetrafluoroethylene, better known as PTFE [4]. As evaporation proceeds, contaminant concentration increases and the particles are left behind on the internal porous media structure. The interplay between transport processes and contaminant deposition in the internal structure of the porous media influence the solvent evaporation rate.

In this work, we consider a porous material that is filled with a liquid solution containing molecules from multiple species with known starting concentrations. As the solvent evaporates, molecules from these species are left behind and deposited on the internal pore walls within the porous material. In the 2020 MPI workshop [4], a model was developed that describes evaporation and deposition in a single cylindrical pore structure. In this year's workshop, we seek to

- Further examine the dependence of the mass distribution of molecules along the pore walls and the drying rate/time on the pore diameter, pore length, fluid wetting properties, and evaporation conditions.
- Extend the model to a porous structure that has a distribution of pore sizes and in which. fluid moves due to capillary force. We investigate different approaches to model this problem including continuum mechanics, network dynamics, and network homogenization.
- Understand how the mass distribution of molecules change upon cycles of wetting and drying.

The report is organized as follows: in §2, we consider the microscale problem of deposition of solute particles within a single representative pore channel. In §3, the motion of a droplet within a pore with sloped sides was modelled. Then, we adopt a homogenization approach to examine macroscopic fluid flow in §4. We develop a model considering a whole porous medium rather than individual pores in §5. In §6, a network approach was developed to examine macroscopic capillary effects. Finally, we summarize our modeling results in §7 and provide some insight into real-world applications as well.

PART ONE
Microscopic models

2 Single pore with evaporation and solute deposition

2.1 Introduction

We consider the microscale problem of deposition of solute particles within a single representative pore channel left as the residue from the evaporation of a volatile fluid solution. Of interest is understanding the forms of contaminant particle distributions on the walls of the pore that can occur and how they can potentially lead to clogging of the

porous material under repeated use. We use a model described in [4, Section 3], developed at the 2020 MPI study group, in which evaporation in porous media was examined.

2.2 Reduced model formulation

The full problem of describing adsorption of contaminants in a porous material from an evaporating liquid solution involves modeling thermodynamic effects, free-surface fluid dynamics, multi-phase fluids, and mass transport. However, by making a set of simplifying assumptions, this system can be reduced to a tractable model. These assumptions are:

(1) The initial state for the model is a pore channel completely filled with fluid. The fluid has a uniform concentration of dissolved contaminant particles.

(2) The pore channel is initially axisymmetric and the axisymmetry of the channel and the particle concentration will be maintained for all times.

(3) The fluid will always assumed to be in the form of a fluid "plug" completely filling the width of the pore channel. There will be no annular two-phase flows, hence the domain occupied by the fluid can be identified by a range along the axis of the pore channel.

(4) For the model in this section, capillary effects yielding a curved meniscus and nontrivial contact angles will be neglected. Wetting properties of the pore channel are neglected. Consequently evaporation will occur through a flat fluid interface.

(5) Transport of the solute across the width of the channel is rapid and can be assumed to be in equilibrium. Using the slenderness of the pore channel the particle concentration can be reduced to studying the cross-sectionally averaged concentration.

(6) The adsorption of particles onto the walls of the pore is due to precipitation out of the fluid. This occurs when the local concentration exceeds a saturation concentration C_{sat}. This deposition process will be treated as being irreversible; deposited particles cannot return to the solution.

(7) Evaporation and deposition are slow processes relative to the fluid flow. So, the carrier fluid will be close to equilibrium on the slow timescale of the dynamics considered. The fluid will be treated as being quasi-steady.

(8) The concentration of solute particles is assumed to be low so the solution can be treated as being dilute and changes in solution volume can be neglected.

(9) The pore channel will be assumed to span the thickness of the layer of the porous material and the fluid will initially fill the entire channel. Using the symmetry of the system, the problem can be solved on half of the length of the channel.

(10) The evaporation rate of the volatile solvent will be assumed to be constant. We will neglect thermodynamic effects from any phase changes or temperature or humidity gradients.

Using the above assumptions, the full governing system can be reduced to a set of coupled differential equations for the height of the fluid column in the pore, $z = h(t)$, the solute particle concentration, $C(z, t)$, and the radius of the pore channel, $R(z, t)$. The system can be non-dimensionalized using lengthscales for the (half)-length of the pore

Figure 1. Schematic representations of the model geometry (cut-away views): (left) the initial state of a liquid-filled uniform pore channel, and (right) at a later time, the partially evaporated fluid and deposited particles (gray) accumulating on the channel walls (black).

channel and a radius of a reference pore. This sets the domain to be $0 \leq z \leq 1$ with $z = 0$ being a plane of symmetry at the middle of the porous material. The height of the fluid free surface will be steadily decreasing as evaporation proceeds, $h(t) \geq 0$. The solute particles rapidly re-equilibrates as the fluid evaporates, $C(z, t)$ is defined on $0 \leq z \leq h(t)$, subject to appropriate boundary conditions on the channel walls and fluid free-surface. See Figure 1 for a sketch of the model geometry. Time is non-dimensionalized by an arbitrary unit of time (e.g. 1 second) to leave open the relations between the timescales for diffusion, evaporation and deposition processes.

The resulting reduced model is as follows. The decreasing height of the fluid column is determined by the evaporation rate E (taken to be a constant),

$$\frac{dh}{dt} = -E, \quad h(0) = 1. \tag{2.1}$$

The radius of the pore will decrease as the particles are deposited onto the wall; this is expressed by the equation

$$\frac{\partial R}{\partial t} = -\chi Q_w(C), \quad 0 \leq z \leq h(t), \tag{2.2}$$

where $\chi > 0$ is a dimensionless volume scaling coefficient and $Q_w \geq 0$ is the precipitation flux. An initial condition describing the initial channel profile must be provided, $R(z, 0) = R_0(z)$ for $0 \leq z \leq 1$ at $t = 0$. Note that no deposition occurs in the region above the evaporation interface, $h(t) < z \leq 1$.

A constitutive relation is needed to describe the flux of material onto the channel walls. Precipitation is modelled as occurring if the local concentration exceeds saturation level C_{sat} with a rate linearly proportional to that difference,

$$Q_w(C) = \lambda(C - C_{\text{sat}})_+, \tag{2.3}$$

with $\lambda > 0$ and the positive truncation defined as $(w)_+ \equiv \max(w, 0)$.

Neglecting convective effects, the mass of particles in solution will be governed by a

transport equation in terms of the cross-sectionally averaged concentration $C(z,t)$,

$$\frac{\partial}{\partial t}(\pi R^2 C) = D\frac{\partial}{\partial z}\left(\pi R^2 \frac{\partial C}{\partial z}\right) - 2\pi R Q_w(C), \quad 0 \le z \le h(t), \tag{2.4a}$$

where D is a diffusion coefficient. We have included factors of π here to make clear the terms involving diffusion along the axis of the channel, involving the varying cross-section of the pore (area πR^2), and the flux of particles onto the channel walls (circumference $2\pi R$). The initial concentration is assumed to be uniform,

$$C(z,0) = C_0, \quad 0 \le z \le 1. \tag{2.4b}$$

At the moving evaporation interface a condition can be derived from a conservation of mass argument for the non-volatile particle concentration to yield the Robin boundary condition,

$$D\frac{\partial C}{\partial z} + \frac{dh}{dt}C\bigg|_{z=h(t)} = 0. \tag{2.4c}$$

Finally, from the assumed symmetry about the middle of the porous layer we write

$$D\frac{\partial C}{\partial z}\bigg|_{z=0} = 0. \tag{2.4d}$$

Consequently, (2.4) is a boundary value problem for a reaction-diffusion equation and occurs within the overall coupled moving boundary problem describing the overall model, (2.1)–(2.4).

The simple evaporation model (2.1) can be solve in closed-form independently of the rest of the model to yield

$$h(t) = 1 - Et, \quad 0 \le t \le t_*, \quad t_* = 1/E. \tag{2.5}$$

This sets the range of times for the dynamics for one wetting cycle of the porous layer. We note that, since the height of the fluid column approaches zero as $t \to t_*$ (and hence the fluid volume goes to zero), the concentration of remaining particles remaining in solution will diverge. The model has not been formulated such that all of these particles are guaranteed to be deposited on the channel wall at $z = 0$ and $t = t_*$. The large concentration also violates assumptions that the model is based on. For these reasons, simulations of the model should only be run on $0 \le t < t_* - \epsilon$ with some $\epsilon > 0$ to avoid generating singularities in the results.

2.3 Computational approach

As evaporation occurs, the height of the fluid decreases as described by (2.1). To implement numerical simulations, we introduce a new variable y defined by

$$z = h(t)y \tag{2.6}$$

with $0 \le y \le 1$ to transform the system into a boundary value problem on a fixed computational domain, $y \in [0,1]$. We let

$$\hat{C}(y,t) = C(z,t), \quad \hat{R}(y,t) = R(z,t) \tag{2.7}$$

and perform the change of variables.

Substituting (2.7) into (2.2), we obtain the evolution equation for the pore radius,

$$\frac{\partial \hat{R}}{\partial t} - \frac{y}{h}\frac{dh}{dt}\frac{\partial \hat{R}}{\partial y} = -\chi Q_w(\hat{C}), \tag{2.8}$$

and substituting (2.7) into (2.4), we obtain the transport problem for the solute concentration

$$\begin{cases} \dfrac{\partial(\hat{R}^2\hat{C})}{\partial t} - \dfrac{y}{h}\dfrac{dh}{dt}\dfrac{\partial(\hat{R}^2\hat{C})}{\partial y} = \dfrac{D}{h^2}\dfrac{\partial}{\partial y}\left(\hat{R}^2\dfrac{\partial \hat{C}}{\partial y}\right) - 2\hat{R}Q_w(\hat{C}), \quad 0 < y < 1, \\ \left[\dfrac{D}{h}\dfrac{\partial \hat{C}}{\partial y} + \dfrac{dh}{dt}\hat{C}\right]_{y=1} = 0, \\ \left.\dfrac{\partial \hat{C}}{\partial y}\right|_{y=0} = 0, \end{cases} \tag{2.9}$$

and equation (2.1) is unchanged. The change of variables has introduced advective derivative terms in (2.8) and (2.9) as well as time-dependent coefficients on some terms. To solve the system (2.8)-(2.9) numerically, and we apply an explicit backward Euler one-step finite difference timestepping method with centered spatial discretization. To discretize the spatial domain $y \in [0, 1]$, we divide it into M subintervals, and denote the gridpoints $y_j = j\Delta y$ by $y_0, y_1, \ldots, y_M$. And we use the superscripts ^{new} and ^{old} to denote the values at new and old times.

From equation (2.1) we have

$$\frac{h^{new} - h^{old}}{\Delta t} = -E. \tag{2.10}$$

For equation (2.8)

$$\frac{\hat{R}_j^{new} - \hat{R}_j^{old}}{\Delta t} + y_j\frac{E}{h^{old}}\frac{\hat{R}_j^{old} - \hat{R}_{j-1}^{old}}{\Delta y} = -\chi Q_w(\hat{C}_j^{old}), \quad j = 1, \cdots, M, \tag{2.11}$$

with $(\hat{R}_0^{new} - \hat{R}_0^{old})/\Delta t = -\chi Q_w(\hat{C}_0^{old})$ for $j = 0$. Since (2.8) has no diffusive term, for numerical stability, (2.11) is written using an upwind spatial discretization. System (2.9) is discretized as

$$\begin{aligned} &\frac{\hat{C}_j^{new}(\hat{R}_j^{new})^2 - \hat{C}_j^{old}(\hat{R}_j^{old})^2}{\Delta t} + y_j\frac{E}{h^{old}}\frac{\hat{C}_{j+1}^{old}(\hat{R}_{j+1}^{old})^2 - \hat{C}_{j-1}^{old}(\hat{R}_{j-1}^{old})^2}{2\Delta y} = \\ &\frac{D}{(h^{old})^2\Delta y}\left(\frac{(\hat{R}_{j+1}^{old} + \hat{R}_j^{old})^2}{4}\frac{\hat{C}_{j+1}^{old} - \hat{C}_j^{old}}{\Delta y} - \frac{(\hat{R}_j^{old} + \hat{R}_{j-1}^{old})^2}{4}\frac{\hat{C}_j^{old} - \hat{C}_{j-1}^{old}}{\Delta y}\right) \\ &- 2\hat{R}_j^{old}Q_w(\hat{C}_j^{old}), \quad j = 1, 2, \cdots, M-1, \\ &\frac{-3\hat{C}_0^{new} + 4\hat{C}_1^{new} - \hat{C}_2^{new}}{2\Delta y} = 0, \\ &\frac{D}{h^{new}}\frac{3\hat{C}_M^{new} - 4\hat{C}_{M-1}^{new} + \hat{C}_{M-2}^{new}}{2\Delta y} - E\hat{C}_M^{new} = 0, \end{aligned} \tag{2.12}$$

Description	**Symbol**	**Value**
Evaporation rate	E	1
Volume scaling coefficient	χ	0.8
Precipitation rate coefficient	λ	1
Saturation concentration	C_{sat}	0.5
Initial concentration	C_0	0.45-0.55
Diffusion coefficient	D	1
Initial radius	R_0	0.1

Table 1. Parameters for numerical simulations

where we have used $h' = -E$. At each timestep, (2.10) is used to obtain h^{new} then (2.11) can be solved for $\hat{R}^{new}$ and finally (2.12) yields $\hat{C}^{new}$. We note that at each t^{new}, $\hat{R}^{new}$ and $\hat{C}^{new}$ provide values for the pore radius R and solute concentration C on the range of the fluid column, $0 \leq z \leq h(t)$. To provide R, C on the entire pore ($0 \leq z \leq 1$), values from previous times and interpolation of y_j values onto equally-spaced z's are used for $0 < t < t_*$.

This numerical scheme was implemented in MATLAB and used to compute all of the figures in this section.

2.4 Results

Our model is based on key parameters for deposition/evaporation and initial conditions for the channel geometry and the solute concentration: the evaporation rate (E), taken to be constant; the deposition coefficient (λ), characterizing the rate of adsorption deposits; volume scaling coefficient (χ); the saturation concentration (C_{sat}); the initial concentration (C_0); the permeability of the porous material can be used to set an effective diffusion coefficient for the channel (D), and a lengthscale characterizing the depth of the pore; the initial radial profile of the channel ($R_0(z)$).

In this section, we investigate the deposition of particles under a constant evaporation rate scenario by varying some of the parameters within our model, notably the initial concentration and some geometrical aspects of the initial radius profile of the pore. We use the parameter values summarized in Table 2.3, which affect the occurrence of deposition. With a constant evaporation rate, varying the concentration of particles within the fluid plug exhibits two main classes of behaviors in the model as depicted in Figures 2 and 3 showing snapshots at the simulation half-time (when half of the channel is still filled with fluid):

(i) When the fluid is initially under-saturated, no precipitation will occur at early times and consequently no particles collect near the pore inlet. Saturation will first be reached

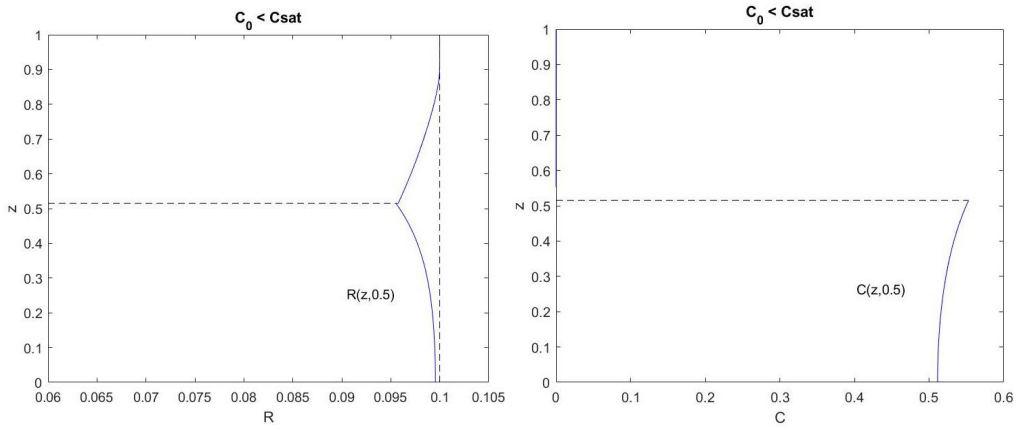

Figure 2. Solution at $t = 0.5$ from an initially under-saturated fluid, $C_0 < C_{\text{sat}} = 0.5$. Left: particle deposition and the narrowing of the pore radius $R(z,t)$. Right: Concentration of particles remaining in the fluid, $C(z,t)$. The horizontal dashed lines show the position of the evaporation interface and height of the fluid remaining.

at the moving evaporation front, with a concentration gradient being driven by the evaporation rate (2.4c).

(ii) In the over-saturated case, deposition of particles begins at the pore inlet. The rate of pore-narrowing is seen to decrease with increasing depth, driven by an overall decrease in concentration due to precipitation over the entire length of the channel.

While the concentration profiles at $t = 0.5$ (shown on the right of both figures) are very similar between the two cases, the radial profile is dramatically different due to the cumulative particle deposition that starts from $t = 0$ in the over-saturated case. The radial profile is frozen above the evaporation interface ($z = h(t)$) but continues to evolve in the part of the channel still containing fluid. Further discussion for the under-saturated and over-saturated regimes are presented in the following sections.

2.4.1 *Under-saturated regime*

In this regime, there is no deposition initially as the particle concentration is uniformly below the saturation level before the evaporation process begins. Deposition occurs when the concentration of particles remaining in the fluid increases to C_{sat} anywhere. As the fluid evaporates, the concentration at the interface, $z = h(t)$, increases until it is greater than saturation, which leads to particles precipitating out and depositing on the channel wall. The pore radius then starts shrinking gradually, first at the evaporation front, where the concentration of particles first reaches the saturation threshold. This behavior is observed in Figure 4, where we set the initial concentration of particles as $C_0 = 0.45$ with the saturation level being $C_{\text{sat}} = 0.5$. Precipitation first occurs when the free surface is located at $z \approx 0.95$ and continues for all later times as evaporation proceeds. For early times, deposition only occurs in a region near the moving interface where the concentration is above saturation. At larger times, evaporation has reduced the volume of

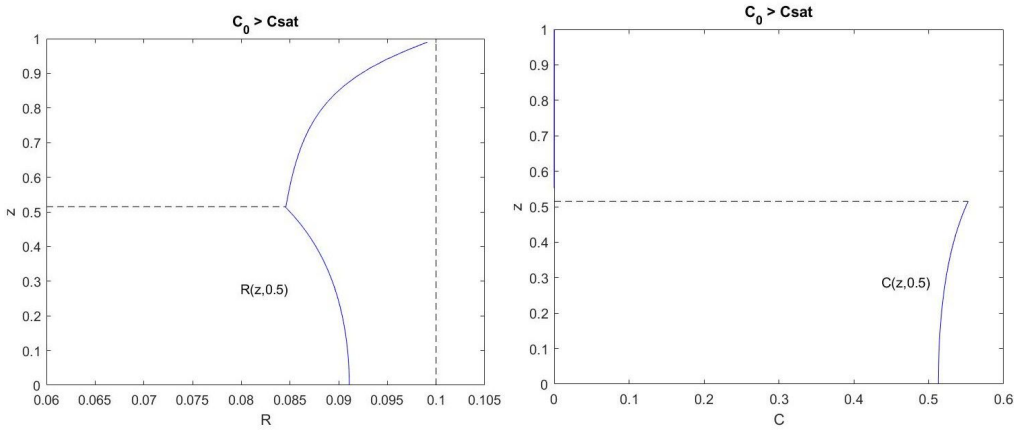

Figure 3. Same as in Figure 2 but for an initially over-saturated fluid, $C_0 > C_{\text{sat}} = 0.5$, showing a dramatically different distribution of deposition on the walls of the channel (Left).

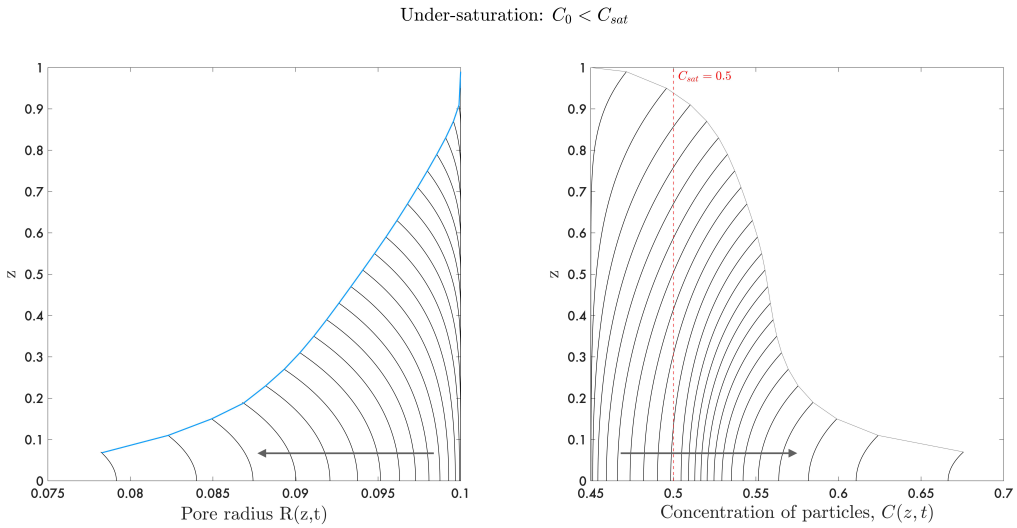

Figure 4. Dynamics for the initially under-saturated case: (Left) Pore radius profiles $R(z,t)$ at a series of successive times. (Right) Concentration profiles $C(z,t)$ at corresponding times.

the fluid enough to make the concentration increase above saturation everywhere, yielding an approximately constant rate of pore-narrowing with increasing depth for much of the following evolution. The overall distribution of deposited particles is a concave-upward profile. The envelope of the $R(z,t)$ curves (shown in blue) gives the static pore profile after all of the fluid has evaporated. We observe that the concentration in the remaining fluid is monotone increasing at each z along the length of the channel.

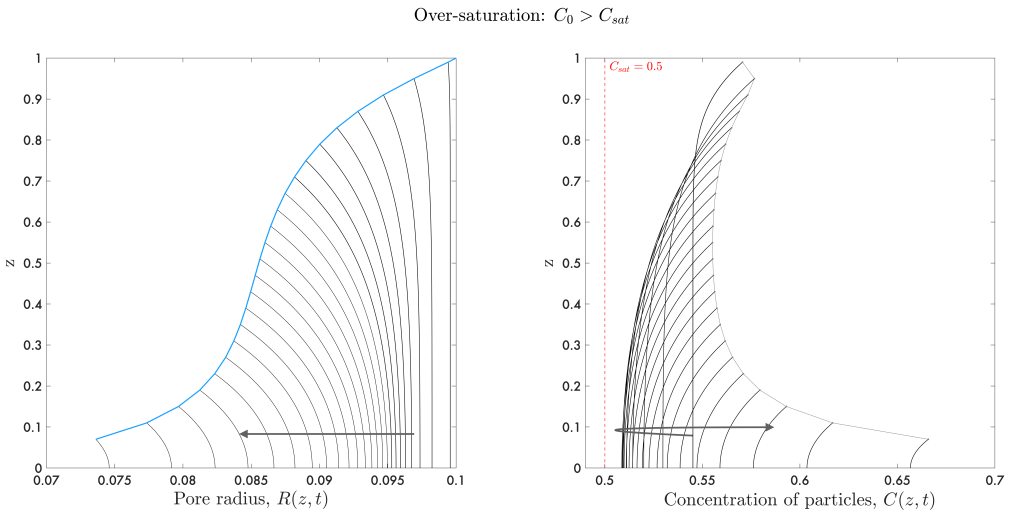

Figure 5. Dynamics for the over-saturated case: (Left) Pore radius profiles $R(z,t)$ at a series of successive times. (Right) Concentration profiles $C(z,t)$ at corresponding times. Arrows indicate the direction of time-evolution, which is non-monotone for the concentration.

2.4.2 *Over-saturated regime*

We now increase the initial concentration to $C_0 = 0.55$ while retaining saturation as $C_{\text{sat}} = 0.5$. In this case, a notably different behavior is seen in Figure 5. The deposition of particles onto the wall over the entire length of the channel begins immediately at $t = 0$. Similar to the under-saturated case, in the initial phase of the dynamics, deposition will occur more rapidly at the evaporation interface than from the bulk of the fluid because the evaporation-driven gradient makes the concentration largest at $z = h$. The influence of this gradient will gradually spread throughout the bulk of the fluid and sets a minimum concentration that occurs in the middle of the pore. The concentration will then exhibit a non-monotone behavior. It will start increasing due to the evaporation having decreased the fluid volume at a greater rate than the flux of particles onto the walls. This behavior is accompanied by a change in the concavity of the pore radius profile.

2.4.3 *Cylindrical vs. conical pores*

Noting that both cases above yielded deposition profiles with narrowing of the pore increasing with distance into the channel, here we want to study the evaporation and deposition process in a conical pore. Having the ability to change the initial pore geometry in the computations is a very helpful feature since the cylindrical pore case, $R_0(z) =$ constant, may be too restrictive/idealized an assumption. We will also use this in another context in the next section.

We consider a pore with initial profile $R_0(z) = 0.1 + 0.1(z - 0.5)$, which is a truncated cone on $0 \le z \le 1$. (Recall that we are assuming symmetry in the porous layer ($-1 \le z \le 1$) across $z = 0$, so this is half of a double-cone.) In Figure 6 we compare the dynamics

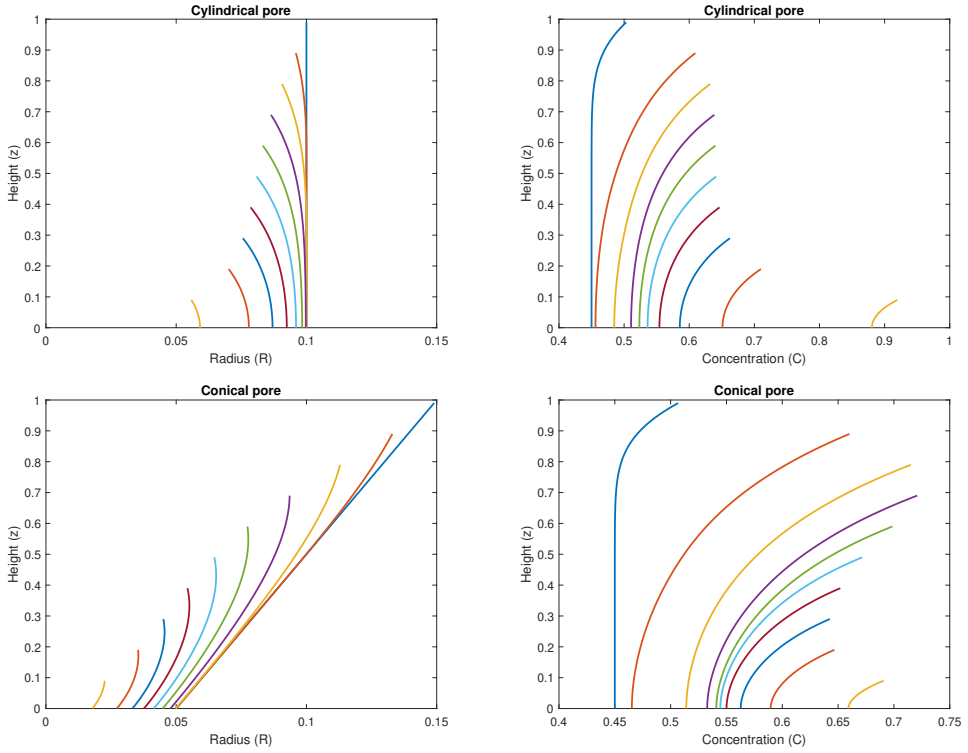

Figure 6. Comparison of deposition dynamics in the initially under-saturated case: (Top row) Cylindrical pore, (Bottom row) Conical pore. Left column shows pore radial profiles. Right column has concentration profiles. System parameters for both were $E = 1, D = 1, \chi = 0.8, \lambda = 1, C_{\text{sat}} = 0.5, C_0 = 0.45$.

in the under-saturated case for this conical pore as compared with the cylindrical pore, $R_0 = 0.1$ (similar to the results shown in Fig. 4). It is interesting to observe that in the conical pore case, the peak concentration (the concentration at $z = h(t)$) has a non-monotone behavior.

2.4.4 *Repeated wetting/drying cycles*

In this section, we further investigate behavior of pore with initially under-saturated fluids by implementing several wetting-drying cycles to gain further insights into controlling deposition leading to clogging within our system. We set the initial radius and concentration to be $R_0 = 1$ and $C_0 = 0.4$, with an increased saturated concentration $C_{\text{sat}} = 0.8$; other parameters have the same values as those in the previous subsection. The radial constriction is similar to the simulation in Figure 4, as expected. As previously discussed, the concentration increases as the fluid evaporates, yielding to deposition increasing with depth in the under-saturated regime. Therefore, the pore shrinks more towards the middle in the first cycle and less at the inlet region. We retain the final pore configuration, $R = R(z, t_*)$ to be the initial profile for the next cycle and flood the pore

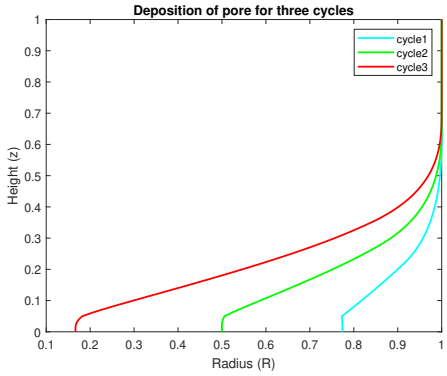

Figure 7. Simulation of radius of a cylindrical pore for three wetting/drying cycles.

with the same fluid for a second and a third wetting/drying cycle. The simulation of the pore radius for three cycles is shown in Figure 7. We see that the deposition behaviour is repeated during subsequent flooding and that the pore is most likely to completely block at $z = 0$. Our modelling assumptions and simulation framework give the cumulative deposition on the channel walls over multiple cycles as added particle layers over previously frozen profiles. Improvements to the model could seek to consider compactification of the previously deposited dry layers and whether some deposits might go back into solution in under-saturated fluids.

2.5 Analysis of a limiting case: large diffusion and small deposition

While the simulation of the model considered here is easy to implement and could parallelized to represent arrays of similar pores subject to different conditions, it would also be helpful to explore whether understanding of some behaviors can obtained analytically without the need for numerical simulations. Here we briefly consider one limiting case where the pore profile can be estimated from a single integration.

Consider the case of small deposition volume per unit of precipitant, $\chi \to 0$, and large diffusion (hence low gradients of concentration in the fluid), $D \to \infty$. For convenience, we link these two effects by writing $D = 1/\chi$ as $\chi \to 0$. Then system (2.2, 2.4) can be written as

$$\frac{\partial R}{\partial t} = -\chi Q_w(C), \tag{2.13a}$$

$$\chi \frac{\partial}{\partial t}(R^2 C) = \frac{\partial}{\partial z}\left(R^2 \frac{\partial C}{\partial z}\right) - 2\chi R Q_w(C), \tag{2.13b}$$

$$\left(\frac{\partial C}{\partial z} - \chi E C\right)\Big|_{z=h(t)} = 0, \qquad \frac{\partial C}{\partial z}\Big|_{z=0} = 0. \tag{2.13c}$$

We can write the solutions as perturbation expansions for $\chi \to 0$,

$$C = C_{(0)} + \chi C_{(1)} + O(\chi^2), \qquad R = R_{(0)} + \chi R_{(1)} + O(\chi^2). \tag{2.14}$$

Then at leading order we get

$$\frac{\partial R_{(0)}}{\partial t} = 0, \qquad \frac{\partial}{\partial z}\left(R_{(0)}^2 \frac{\partial C_{(0)}}{\partial z}\right) = 0, \quad C_{(0),z}(h,t) = 0, \quad C_{(0),z}(0,t) = 0. \tag{2.15}$$

From the first equation we get that the channel profile will remain close to the initial condition, $R \sim R_0(z)$. The boundary value problem for $C_{(0)}$ then determines the leading order concentration to be spatially uniform on $0 \le z \le h(t)$. To be consistent with conservation of mass at leading order, this should be

$$C_{(0)}(t) = \frac{C_0 V_0}{\pi \int_0^{h(t)} R^2(z,t)\, dz}, \tag{2.16}$$

where $V_0 = \pi \int_0^1 R_0^2\, dz$ is the initial volume of the filled pore. To leading order, the integrand in the dynamic volume (in the denominator) can make use of $R \sim R_0(z)$.

Going on to $O(\chi)$ we get the equations

$$\frac{\partial R_{(1)}}{\partial t} = -Q_w(C_{(0)}), \tag{2.17a}$$

$$R_0^2 \frac{\partial C_{(1)}}{\partial t} = \frac{\partial}{\partial z}\left(R_0^2 \frac{\partial C_{(1)}}{\partial z}\right) - 2R_0 Q_w(C_{(0)}), \tag{2.17b}$$

$$\left(\frac{\partial C_{(1)}}{\partial z} - EC_{(0)}\right)\Big|_{z=h(t)} = 0, \quad \frac{\partial C_{(1)}}{\partial z}\Big|_{z=0} = 0. \tag{2.17c}$$

The evolution equation for $C_{(1)}(z,t)$ is a reaction-diffusion initial-boundary value problem similar to the structure of of the original full system, except that the pore radius is fixed.

We can re-write the equation for the evolution of the pore radius (2.17a) as

$$\frac{\partial R_{(1)}}{\partial t} = -\lambda(C_{(0)}(t) - C_{\rm sat})H(C_{(0)}(t) - C_{\rm sat})H(h(t) - z), \tag{2.18}$$

where $H(x)$ is the Heaviside step function, eliminating deposition unless $C_{(0)} > C_{\rm sat}$ and $z < h(t)$.

As a simple example of solving this model, for convenience take $\lambda = E = 1$ and the initial pore radius to be $R_0(z) = 1$. This yields $h(t) = 1 - t$ on $0 \le t < 1$ and (2.18) reduces to

$$\frac{\partial R_{(1)}}{\partial t} = -\left(\frac{C_0}{1-t} - C_{\rm sat}\right) H\left(\frac{C_0}{1-t} - C_{\rm sat}\right) H(1 - t - z). \tag{2.19}$$

There are two cases to be considered based on whether the initial concentration is above or below the saturation level. In the super-saturated case, $C_0 > C_{\rm sat}$ and there will be deposition of particles on the entire range of the pore wall, $0 \le z \le 1$, for the whole range of time, $0 \le t < 1$. In the under-saturated case there will be no deposition of particles until enough of the fluid solution has evaporated to raise the concentration to the saturation level, $\bar{C}(t_0) = C_{\rm sat}$, namely

$$t_0 = 1 - \frac{C_0}{C_{\rm sat}} > 0. \tag{2.20}$$

Then deposition will occur on the range $0 \le z \le h(t_0) = C_0/C_{\rm sat}$ (with $R(z,t) = R_0(z)$

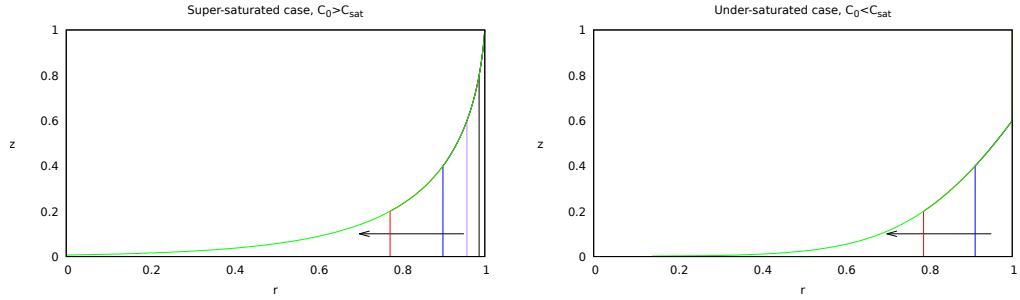

Figure 8. Evolution of the pore radius profile in the super-saturated (left) and under-saturated (right) cases predicted by in the diffusion-dominated regime.

for $h(t_0) < z \leq 1$) over the range of times $t_0 \leq t < 1$. We integrate (2.19) to find that

$$R(z,t) \sim 1 + \chi \left(C_0 \ln(1-t) + C_{\text{sat}} t \right) \Big|_{t_0}^{\min(t,1-z)} . \tag{2.21}$$

Both cases can be covered by this result by defining $t_0 = 0$ when we are in the super-saturated case. The steady pore channel profile (after all of the fluid has evaporated, $t > 1$) is given by

$$R(z) \sim 1 + \chi \left(C_0 \ln \left(\frac{z}{1-t_0} \right) + C_{\text{sat}} (1 - z - t_0) \right) , \tag{2.22}$$

see Figure 8. In both cases, the steady profile has the channel being clogged as $z \to 0$. However, our asymptotic solutions break down in this limit and so further work must be done to examine this behavior.

2.6 Directions for further work

The simple single-pore model considered in this section is a very easy-to-implement simulation testbed that can be used to explore deposition behavior in many limiting cases (and serve as building blocks for scaling-up to larger network or homogenized systems). There are many directions for further studies, some of which are explored in the other sections of this report.

Some of the specific directions for extending the single pore model include:

- Free-boundary geometry: making the evaporating interface curved would allow for the incorporation of capillary effects, including wetting properties of the porous material, as will be done for the case without particle transport in §3.
- Evaporation rate: a better treatment of how thermodynamics/phase change/heat transfer and humidity influence the evaporation rate is needed [21, 30, 33]. Interface evaporation models using stagnant gas-phase layer approaches from the engineering literature [3] could be incorporated. However, those simple models require modeling the concentration of vapour outside the pore.
- Fluid dynamics: a better treatment of how the fluid dynamics influences the distribution of particle deposition on the pore wall [12].

- Non-dilute solutions: a better description of the properties of fluids containing particles is needed, eg [22],[18].
- Explicit solutions: Further work is needed on analysis of different limiting cases for the model. In the case when the change of radius due to deposition is quite small compared to the radius itself, and when the convective velocity is known or is dominated by diffusion, we may solve the (moving) boundary problem for the linear diffusion equation assuming that radius as a function of height is known. We may then extract the boundary data needed to compute the contaminant flux and its deposition rate on the walls and, from that, a correction to the radius (assumed to be small). It is then possible to iterate the process using updated radius. One related observation can be made. The equation for the radius (2.8) in the numerical formulation is a linear, scalar PDE for R and if concentration is known, it can be integrated by the method of characteristics. However, once this is done, the diffusion equation for concentration becomes nonlinear, and with a delay term present as the true radius depends on concentration past history.

3 A simple model for the motion of an evaporating droplet of liquid in a converging pore

We next consider the motion of a droplet within a pore with sloped sides, as shown in Figure 9. Throughout this section we use lowercase fonts to denote dimensional quantities; uppercase fonts, introduced subsequently in §3.2, will be dimensionless. We restrict our attention to the case where there are no particles present and we suppose that the droplet is two-dimensional and contains Newtonian liquid with constant viscosity μ. We assume that the droplet is held between two plates, each tilted at a small angle β to the longitudinal axis, as shown in figure 9, to make an symmetric diverging pore. We suppose that, initially, the droplet has length $2L$ and is centred at the place where the pore has width 2λ, and that $L \gg \lambda$. Locating the origin of our coordinate system at the middle of the initial location of the droplet, we write the equation of the pore walls at $x = \pm f(z)$ as

$$f = \lambda + z \tan\beta. \tag{3.1}$$

We assume that the liquid is pore-materialo-phobic and that, throughout the motion, the air-liquid interfaces are spherical caps which make constant contact angle $\alpha + \pi/2$ with the pore walls[1], as shown in Figure 9. Using elementary geometry, we find that the radii of curvature, $r^{\pm}$, (where the $^+$ denotes the longer meniscus, and $^-$ denotes the shorter meniscus) of the menisci are

$$r^{\pm} = \frac{(\lambda \pm z_w^{\pm} \tan\beta)}{\sin(\alpha \pm \beta)}, \tag{3.2}$$

where $z_w^{\pm}(t)$ are the locations of the contact lines on the pore wall. Providing $\beta \neq 0$, the radii given by (3.2) are different and so we expect that the (capillary) pressures generated by the two menisci will be different and this will drive the motion of the droplet. Our final assumptions are that evaporation occurs at the air-liquid interfaces, at speed $E^{\pm}$, and that gravity may be neglected. Our aim in the remainder of this section is to build

[1] Of course, there are numerous more complicated contact line models that we could have imposed.

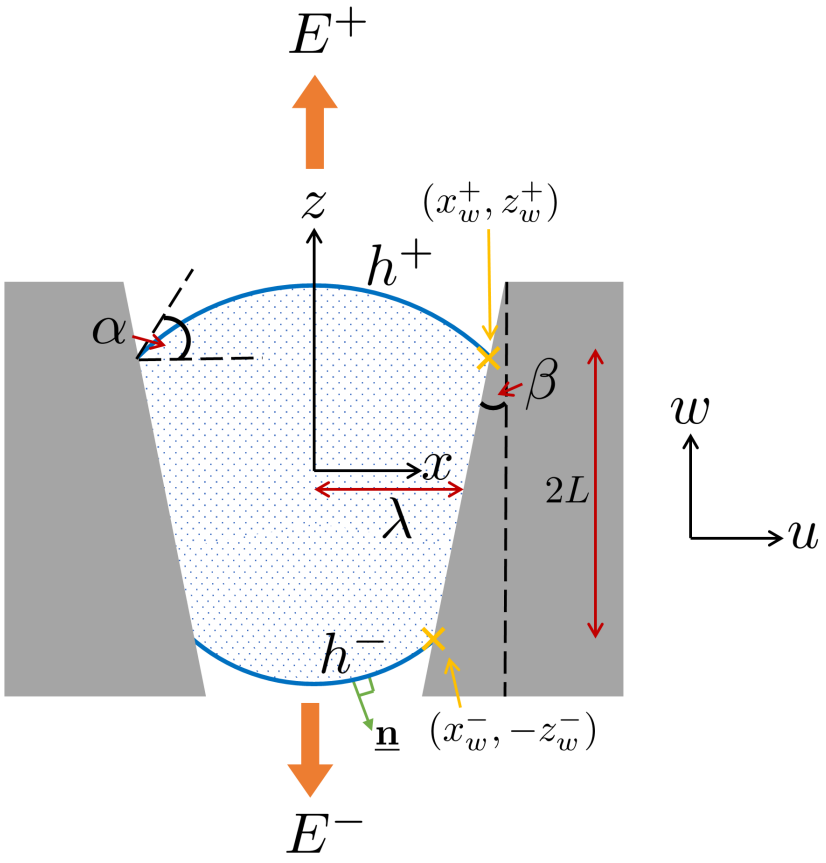

Figure 9. Schematic showing the initial location of the droplet inside a converging pore.

and solve a simple mathematical model for the motion of the droplet in order to study the interplay between capillary and evaporative effects.

3.1 Mathematical model

We suppose that the flow of liquid in the droplet is slow and so the governing equations for the velocity $\boldsymbol{u} = (u, w)$ and pressure p are the continuity and Stokes equations

$$0 = \nabla \cdot \boldsymbol{u}, \tag{3.3}$$

$$0 = -\nabla p + \mu \nabla^2 \boldsymbol{u}. \tag{3.4}$$

At the pore walls located at $x = \pm f(z, t)$, we apply the conditions of no slip ($\boldsymbol{u} \cdot \mathbf{t} = 0$; $\mathbf{t}$ is the unit tangent along the pore wall) and no penetration ($\boldsymbol{u} \cdot \mathbf{n} = 0$; $\mathbf{n}$ is the unit outward-pointing normal to the pore wall), which reduce to

$$u = w = 0 \qquad \text{at} \qquad x = \pm f. \tag{3.5}$$

At the air-liquid interfaces[2], we assume continuity of normal stress and so we write

$$p - p_0 = \frac{\gamma}{r^{\pm}} = \frac{\gamma \sin(\alpha \pm \beta)}{\left(\lambda \pm z_w^{\pm} \tan\beta\right)} \qquad \text{at} \qquad z = \pm z_w^{\pm}, \tag{3.6}$$

where p_0 is the atmospheric pressure and γ is the surface tension. We further pose that the contact lines move according to an ad hoc averaged kinematic condition which we write as

$$\frac{\mathrm{d}z_w^{\pm}}{\mathrm{d}t} = \pm\bar{w} - E^{\pm} \qquad \text{at} \qquad z = \pm z_w^{\pm}, \tag{3.7}$$

where $\bar{w}$ is the cross-sectionally averaged longitudinal velocity. Finally, the initial conditions are that

$$z_w^{\pm} = \pm L \qquad \text{at} \qquad t = 0. \tag{3.8}$$

3.2 Non–dimensionalization

Writing $\delta = \lambda/L \ll 1$, we non–dimensionalize the our model using the following scalings:

$$\begin{gathered} x = \delta L X, \quad z = LZ, \quad t = \frac{L\mu}{\delta\gamma_0} T, \quad u = \frac{\gamma\delta^2}{\mu} U, \quad w = \frac{\delta\gamma}{\mu} W, \\ p - p_0 = \frac{\gamma}{\delta L} P, \quad f(z) = \delta L F(Z), \quad z_w^{\pm} = L Z_w^{\pm}, \end{gathered} \tag{3.9}$$

where we have picked the velocity and pressure scales to balance the capillary terms and the pressure gradient along the droplet with the viscous stress across the droplet. We note that, with these scalings the dimensionless equation (3.1) describing the pore wall becomes

$$F = 1 + \chi Z, \tag{3.10}$$

where $\chi = (\tan\beta)/\delta$. To be consistent with the pore being long and thin, we must have β at most $O(\delta)$. Applying (3.9) to (3.3)–(3.8), we find that the dimensionless governing equations are:

$$0 = \frac{\partial U}{\partial X} + \frac{\partial W}{\partial Z}, \tag{3.11}$$

$$0 = -\frac{\partial P}{\partial X} + \delta^2 \frac{\partial^2 U}{\partial X^2} + \delta^4 \frac{\partial^2 U}{\partial Z^2}, \tag{3.12}$$

$$0 = -\frac{\partial P}{\partial Z} + \frac{\partial^2 W}{\partial X^2} + \delta^2 \frac{\partial^2 W}{\partial Z^2}, \tag{3.13}$$

with boundary conditions

$$U = W = 0 \qquad \text{at} \qquad X = \pm F, \tag{3.14}$$

$$P = \frac{\sin(\alpha \pm \beta)}{1 \pm \chi z_w^{\pm}} \qquad \text{at} \qquad Z = \pm Z^{\pm}, \tag{3.15}$$

$$\frac{\mathrm{d}Z_w^{\pm}}{\mathrm{d}T} = \pm\bar{W} - \mathcal{E}^{\pm} \qquad \text{at} \qquad Z = \pm Z^{\pm}, \tag{3.16}$$

[2] Strictly speaking, we should apply continuity of normal and tangential stresses and a kinematic condition at these interfaces. However, in the long-thin-pore limit we require fewer boundary conditions.

and initial conditions

$$Z_w^{\pm} = \pm 1 \qquad \text{at} \qquad T = 0, \tag{3.17}$$

where $\bar{W}$ is the dimensionless cross-sectionally averaged velocity, and $\mathcal{E}^{\pm} = \mu E^{\pm}/\delta\gamma$.

3.2.1 *Leading order behaviour*

In the limit $\delta \to 0$, the leading-order-in-δ version of (3.12) tells us that $P = P(Z,T)$. We then integrate the leading-order-in-δ version of (3.13) and apply (3.14) to find that

$$W = -\frac{\partial P}{\partial Z}\left(\frac{F^2 - X^2}{2}\right). \tag{3.18}$$

Thus, we find that the cross-sectionally averaged velocity, $\overline{W}$, is given by

$$\overline{W} = \frac{1}{2F(Z)}\int_{-F(Z)}^{F(Z)} W \, \mathrm{d}X = -\frac{1}{3}\frac{\partial P}{\partial Z}F^2. \tag{3.19}$$

Integrating (3.11) across the pore and applying (3.14) we find that

$$\frac{\partial}{\partial Z}\left(\frac{2}{3}F^3\frac{\partial P}{\partial Z}\right) = 0. \tag{3.20}$$

We solve (3.20) and apply the boundary conditions (3.15) to find that

$$P = \frac{\sin(\alpha+\beta)}{1+\chi Z_w^+} + \left(\frac{\sin(\alpha+\beta)}{1+\chi Z_w^+} - \frac{\sin(\alpha-\beta)}{1-\chi Z_w^-}\right)\left(\frac{\frac{1}{(1+\chi z)^2} - \frac{1}{(1+\chi Z_w^+)^2}}{\frac{1}{(1+\chi Z_w^+)^2} - \frac{1}{(1-\chi Z_w^-)^2}}\right). \tag{3.21}$$

We substitute (3.21) into (3.19) to find that

$$\bar{W} = \frac{2\chi}{3\,(1+\chi Z)}\left(\frac{\frac{\sin(\alpha+\beta)}{1+\chi Z_w^+} - \frac{\sin(\alpha-\beta)}{1-\chi Z_w^-}}{\frac{1}{(1+\chi Z_w^+)^2} - \frac{1}{(1-\chi Z_w^-)^2}}\right), \tag{3.22}$$

which we substitute into (3.16) to find

$$\frac{\mathrm{d}Z_w^{\pm}}{\mathrm{d}T} = \pm\frac{2\chi}{3\left(1\pm\chi Z_w^{\pm}\right)}\left(\frac{\frac{\sin(\alpha+\beta)}{1+\chi Z_w^+} - \frac{\sin(\alpha-\beta)}{1-\chi Z_w^-}}{\frac{1}{(1+\chi Z_w^+)^2} - \frac{1}{(1-\chi Z_w^-)^2}}\right) - \mathcal{E}^{\pm}. \tag{3.23}$$

We see immediately that, when $\beta = 0$ (which also forces $\chi = 0$), the pressure in the droplet is constant and there is no flow, as one would expect in this case. Indeed, in this case the solution to the problem is trivial and is given by

$$Z_w^+ = 1 - \mathcal{E}^+ T, \qquad Z_w^- = 1 - \mathcal{E}^- T, \tag{3.24}$$

and the droplet completely evaporates away at the critical time T_c given by $T_c = 2/(\mathcal{E}^+ + \mathcal{E}^-)$ (*i.e.* when $Z^+ = -Z^-$).

We have thus reduced the problem for the motion of the droplet to solving (3.23) for the motion of the two ends of the droplet, subject to the initial conditions given by (3.17).

3.3 Results

We now explore the behaviour of the system. We solve (3.23) and (3.17) numerically using the built-in Mathematica [11] function *NDSolve*. There are five dimensionless parameters in the problem, namely α, β, $\chi(=\tan\beta/\delta)$, and $\mathcal{E}^{\pm}$. We assume for illustrative purposes that $\alpha = \pi/6$ and that $\delta = 0.1$ and we set $\mathcal{E}^{+} = \mathcal{E}^{-} = \mathcal{E}$. We then explore the behaviour of the system as we vary β and $\mathcal{E}$. We take care to ensure that we keep β small enough that the pore walls do not cross.

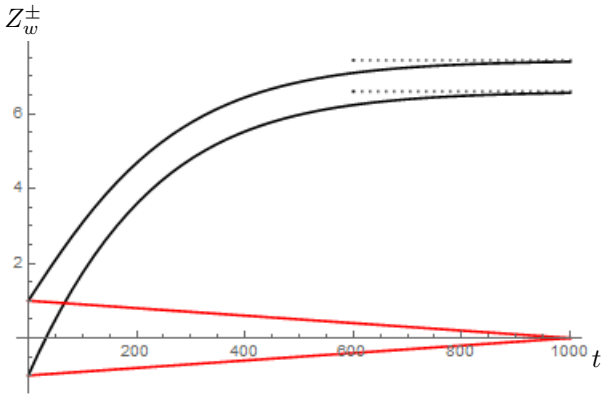

Figure 10. Graph showing the location of the menisci versus time for $\beta = 0$, $\mathcal{E} = 0.001$ (red) and $\beta = 0.02$, $\mathcal{E} = 0$ (black). The dotted lines are the steady state locations of the menisci. The other parameters are $\alpha = \pi/6$ and $\delta = 0.1$.

We first consider setting one of β and $\mathcal{E}$ equal to zero, and we show the evolution of the droplet position in figure 10, picking the nonzero parameter so that the motion occurs over the same time scale in each case. We see that, when $\beta = 0$ (shown in red) we recover the solution presented in (3.24) and the droplet merely shrinks symmetrically due to evaporation. Conversely, when $\mathcal{E} = 0$ (shown in black), we see that the droplet translates towards the diverging end of the pore, shrinking in length as it does (since the pore gets wider). We also see that it slowly settles to a steady state. We note that, when $\mathcal{E} = 0$, we may combine (3.23) and integrate to find that

$$\left(1 + \chi Z_w^{+}\right)^2 - \left(1 - \chi Z_w^{-}\right)^2 = 4\chi, \tag{3.25}$$

which we use as a double check on our numerics in this case. In steady state, we also have that

$$\frac{\sin(\alpha + \beta)}{1 + \chi Z_w^{+}} = \frac{\sin(\alpha - \beta)}{1 - \chi Z_w^{+}}. \tag{3.26}$$

We solve (3.25)-(3.26) to find that, in steady state,

$$Z_w^+ = \frac{1}{\chi}\left(2\sqrt{\frac{\chi}{1-\left(\frac{\sin(\alpha-\beta)}{\sin(\alpha+\beta)}\right)^2}} - 1\right), \tag{3.27}$$

$$Z_w^- = \frac{1}{\chi}\left(1 - 2\left(\frac{\sin(\alpha-\beta)}{\sin(\alpha+\beta)}\right)\sqrt{\frac{\chi}{1-\left(\frac{\sin(\alpha-\beta)}{\sin(\alpha+\beta)}\right)^2}}\right). \tag{3.28}$$

We show these steady state values as dotted lines in figure 10.

Next we first vary β, assuming that $\mathcal{E} = 0.01$ (so that, in the $\beta = 0$ case, the droplet disappears at $T = 100$). In figure 11, we show the motion of the ends of the droplet for $\beta = 0$, 0.01, and 0.02. When $\beta > 0$, we see that the air-liquid interfaces initially towards the diverging end of the channel, and that the lower meniscus moves faster than the upper meniscus. Later in the motion, the direction of travel changes and the speed of each menisci then decreases rapidly until the droplet dries out completely, at a smaller value of T_c than in the $\mathcal{E} = 0$ case. This is because, under our assumption of constant evaporation rate, the mass loss through the menisci is greater when the menisci are longer, as is the case when they move towards the diverging end of the channel. As β increases, we see that the menisci move faster upwards initially, then move further towards the convergent end of the channel during the late stages of the motion, with a corresponding shortening of the lifetime, T_c, of the droplet. We note that, of course, our model is only valid while the droplet retains its small aspect ratio and thus the late-stage behaviour is likely to be modified by two-dimensional effects.

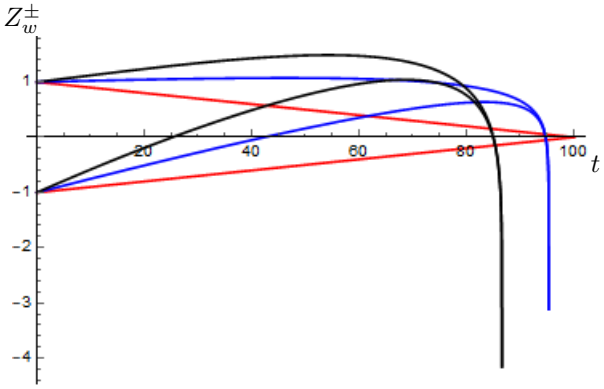

Figure 11. Graph showing the location of the menisci versus time for $\beta = 0$ (red), $\beta = 0.01$ (red), and $\beta = 0.02$ (black). The other parameters are $\alpha = \pi/6$, $\delta = 0.1$ and $\mathcal{E} = 0.01$.

Next we consider the effect of changing $\mathcal{E}$ while keeping $\beta = 0.01$. In figure 12, we show the motion of the ends of the droplet for $\mathcal{E} = 0$, 0.001, and 0.002. We see that, when there is no evaporation, the droplet moves towards the divergent end of the pore and reaches a steady state. As we increase $\mathcal{E}$, we see that evaporation causes the droplet to disappear

in finite time, T_c, with T_c decreasing as $\mathcal{E}$ increases. We also see that evaporation causes the droplet to change direction, as in the previous results. We also show that, for the evaporation rates shown, the droplet appears to always recede to the closed end of the pore (shown as a dashed line), although again we note that the model is invalid as the droplet length tends to zero.

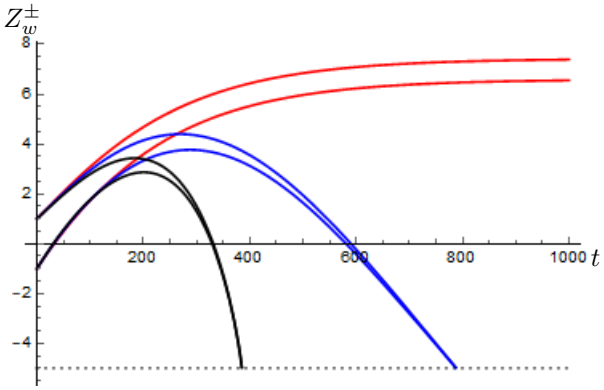

Figure 12. Graph showing the location of the menisci versus time for $\mathcal{E} = 0$ (red), 0.001 (blue), and 0.002 (black). The other parameters are $\alpha = \pi/6$, $\delta = 0.1$ and $\beta = 0.02$. The dashed line indicates the position at which the pore closes.

3.4 Next steps

There are four key next steps. Firstly, we should make the ad hoc kinematic conditions given by (3.7) more realistic, by systematically averaging the *actual* kinematic conditions

$$w = \frac{\partial h^{\pm}}{\partial t} + u\frac{\partial h^{\pm}}{\partial x} - E^{\pm} \qquad \text{on} \qquad z = h^{\pm}(x,t). \tag{3.29}$$

The resulting boundary condition is likely to better capture the motion of the ends of the droplet. Secondly, we should exploit the fact that β is small to simplify the algebra. Thirdly, we should explore the behaviour of the 2-d (not long-thin) system as the droplet evaporates to zero. Finally, we should incorporate particle transport and deposition. This will be non-trivial, since the radii of the menisci will vary with the *local* slope of the substrate which will alter due to particle deposition, building on the model presented in §2.

Of course, there's plenty of additional physics that we could also build into the model such as gravity, better contact line dynamics, or non-Newtonian behaviour, but our simple model gives an indication that there will be interesting dynamics as particle-laden liquids evaporate inside pores.

4 Homogenization approach to examine macroscopic fluid flow

We suppose that the filter is made from a periodic microstructure of horizontal fibers, and for now assume that they are parallel, so that we have a two-dimensional problem

with say a square or hexagonal lattice. Dalwadi et al. (2016; hereafter DBG) [7] consider a filtration problem that is very similar, with a contaminant adsorbing onto the fibers, which act as obstacles in the fluid flow.

We assume that the microscale is saturated with liquid and our model for the liquid flow and evolution of the concentration of particles are the Stokes equations and the advection-diffusion equation, so we write

$$0 = -\boldsymbol{\nabla} p + \mu \nabla^2 \boldsymbol{u}, \qquad \boldsymbol{\nabla} \cdot \boldsymbol{u} = 0, \tag{4.1}$$

and

$$c_t + \boldsymbol{\nabla} \cdot (\boldsymbol{u} c - D \boldsymbol{\nabla} c) = 0. \tag{4.2}$$

Our notation is standard, with $\boldsymbol{u}$ and p denoting the liquid velocity and pressure, respectively, c the concentration of the contaminant, μ the dynamic viscosity, and D the diffusivity of the contaminant in the fluid.

4.1 Boundary conditions on fibers

We need boundary conditions at the interface between fluid and fibers, as well as at the evaporation front. DBG consider circular obstacles of radius $R(t)$, and end up with conditions that can be written as

$$\boldsymbol{u} = R_t \mathbf{n}, \qquad \gamma c = D \frac{\partial c}{\partial n}, \qquad R_t = -V_m D \frac{\partial C}{\partial n}. \tag{4.3}$$

on the interface $r = R(t)$ (the normal here points out, which is the opposite of DBG). The constant γ is an adsorbtion coefficient and V_m is the molar volume of the contaminant (volume of contaminant per mole of contaminant). These three equations come from the no-slip boundary condition, conservation of contaminant (moles per cubic meter) and conservation of mass.

Based on discussions last year, we have been examining the following set of boundary conditions. Consider the flux of mass through a solidifying interface. We have

$$\rho_L (u_{Ln} - V_n) = \rho_S (u_{Sn} - V_n), \tag{4.4}$$

where L and S represent liquid and solid phases, u_n is the normal velocity and V_n is the normal velocity of the interface. We write $\dot{S} = V_n$ and take $u_S = 0$, so that there is no motion of the solid. From now on write $u_L = u$, then

$$u_n = \left(1 - \frac{\rho_S}{\rho_L}\right) \dot{S}. \tag{4.5}$$

For example, if $\rho_S > \rho_L$, then as the contaminant is solidifying, it takes up less space as the solid density is higher, so there must be an inflow of mass through the fluid (i.e. u_n and $\dot{S}$ have opposite sign). Here ρ_S and ρ_L are total densities, so ρ_L includes solvent and solute molecules.

Conservation of dissolved species, assuming no diffusion in the solid, gives

$$c_L (u_n - V_n) - D \frac{\partial c_L}{\partial n} = -c_S V_n. \tag{4.6}$$

At the interface, we match chemical potentials to get $c_S = f(c_L)$. Taking the concentra-

tion at which material precipitates to be $c_L = c_L^*$; there is a corresponding $c_S^* = f(c_L^*)$. We can now return to the notation c for the concentration in the liquid and obtain

$$c = c_L^*, \qquad c^* u_n + \dot{S}(f(c_L^*) - c_L^*) - D\frac{\partial c}{\partial n} = 0, \tag{4.7}$$

on the moving boundary.

The boundary conditions (4.3) and (4.7) are not the same, because the physics of adsorbtion and precipitation/solidification differ. However, we can write them in a unified way as

$$\boldsymbol{u} = \nu_1 \dot{S}\mathbf{n}, \qquad c - c_L^* = -\nu_2 D\frac{\partial c}{\partial n}, \qquad \dot{S} = \nu_3 D\frac{\partial c}{\partial n}. \tag{4.8}$$

The constants ν_1, ν_2 and ν_3 can be matched to DBG ($\nu_1 = 1$, $c_L^* = 0$, $\nu_2 = \gamma^{-1}$, $\nu_3 = V_m$) and to MPI2020 ($\nu_1 = 1 - \rho_S/\rho_L$, $\nu_2 = 0$, $\nu_3 = [f(c_L^*) + c_L\rho_S/\rho_L]^{-1}$). It is convenient to write ν_2 rather than γ since it is the limit $\nu_2 \to 0$ that recovers MPI2020. We could also consider replacing c_L^* by 0, since the advection-diffusion equation only involves derivatives of c, but the resulting negative concentrations might be confusing.

Last year a flux condition of the form

$$\gamma(c - c_L^*)_+ = D\frac{\partial c}{\partial n}, \tag{4.9}$$

was used, where $()_+$ indicates that there is no precipitation unless the boundary concentration is greater than c_L^*. This is a nonlinear boundary condition. DBG mention the possibility of carrying such terms through the homogenization process, in which case they function like an on-off switch on macroscale timescales, but this will not be pursued further here.

4.2 Evaporating boundary

At the evaporating boundary, conservation of c-flux gives

$$-D\frac{\partial c}{\partial n} + c(u_n - V_n) = 0, \tag{4.10}$$

where the normal points out of the fluid. Mass conservation, replacing the details of the flux in the gas phase by an evaporation rate E, gives

$$\rho_L(u_n - V_n) = E\rho_L. \tag{4.11}$$

For simplicity, we take E to be constant. Combining these two conditions gives $u_n - V_n = E$, so that

$$w = \frac{\mathrm{D}h}{\mathrm{D}t} + E, \tag{4.12}$$

where the interface is at $z = h(x, y, t)$. We also find that

$$-D\frac{\partial c}{\partial n} + cE = 0, \tag{4.13}$$

as used in §2, albeit in the no-flow case. Since we are treating the evaporation front as separating the fluid layer from the gas, we also write down a dynamic boundary condition

or stress balance there. For a Stokesian fluid, this corresponds to [13, 19]

$$(p - p_a + \kappa T)n_i = \partial_{s,i}\sigma + 2\mu e_{ij}n_j, \tag{4.14}$$

where p_q is the gas pressure at the interface (atmospheric), κ is the interface curvature, σ is the surface tension, e_{ij} is the velocity gradient tensor and ∂_s represents the derivative along the surface. The term with the gradient corresponds to Marangoni effects when surface tension varies with temperature, which we ignore.

4.3 Initial conditions

Initially, we assume that liquid fills the whole of the filter, which has thickness H, and that the concentration of particles has a constant value. Thus we write

$$h = H, \quad c = C_0 \qquad \text{at} \qquad t = 0. \tag{4.15}$$

4.4 Non-dimensionalization

We follow DGB and non-dimensionalize lengths with H, velocities by U (to be set), the time-dependent fiber radius by δH, concentration by C_0 and pressure by $\mu U\delta^2/H$. The pressure scale balances the pressure gradient on the macroscale to viscous stresses over the microscale; this will enable us to utilise δ^2 in our homogenization procedure. If we follow DBG, we pick the time scale to balance obstacle growth with contaminant concentration, giving $c_0\nu_3/(\delta H\nu_2)$.

The result is essentially the same set of equations as in DBG, with the following differences: the normal points in the other direction, so (2.7c) of DBG becomes

$$\boldsymbol{u} = \nu_1\delta\alpha\frac{\partial R}{\partial t}\mathbf{n}, \tag{4.16}$$

while (2.8b) becomes

$$\delta(c - c^*) = m\mathrm{Pe}^{-1}\frac{\partial c}{\partial n}, \tag{4.17}$$

where $m = \delta U\nu_2$ and $\alpha = c_0\nu_3/(\delta U\nu_2)$.

The natural choice for the velocity scale is E, but we leave it unspecified for now. Our goal is to treat deposition as the process that the timescale that we care about, but it may be convenient to set the velocity scale so that deposition is a slow process.

4.5 Homogenization

The homogenization calculation of DBG should carry through with minor changes in notation, so we can recycle their results with appropriate modifications. The remaining major question is how to handle the drying front. Luckins *et al.* (2019; hereafter LBGW) [16] look at the motion of a front through a similar system, and find that they have to resolve a boundary layer close to the front in order to match between the microscale dynamics and the macroscale domain. We ask "Can one use their approach when the

front is now an evaporation front rather than where a chemical reaction takes place?". However, the physics at the front is not quite the same.

At this point, the framework has been put in place with the detailed algebra remaining to be performed. Some issues to keep in mind are the following:

- Is there any fluid flow? This may seem like a naive questions, but in the case without any microstructure, a homogeneous vertical layer can just evaporate without any fluid motion. Here, however, the microstructure should break the condition $\partial w/\partial z = 0$ and hence lead to flow. While there may meniscus or surface tension effects at the drying front, they should not affect this conclusion.
- Are the DBG scalings compatible with the intermediate asymptotic regime used in LBGW to describe the interface's motion through the microscale?
- Is there a natural velocity scale that has been neglected? If there is, then E/U measures the speed of evaporation. If that is slow, presumably the system evolves through a system of quasi-steady states. If it is large, then the interface moves faster than the particles are deposited, but eventually c must become large enough for the deposition to happen as quickly. Otherwise the liquid would become supersaturated.
- What about multiple drying cycles? The natural approach is start the simulation from the previous end condition. This assumes that the particles do not re-enter the suspension as the membrane is wetted anew.

4.6 Homogenized equations

The resulting macroscale equations are a combination of DBG and LBGW. The dependent variables are functions of the slow variables $\mathbf{X}$ and T. The Stokes equations will lead to Darcy's law in the form

$$\boldsymbol{u} = -\mathcal{K}(\phi)\boldsymbol{\nabla} p, \tag{4.18}$$

where $\mathcal{K}(\phi)$ is a scalar function encoding the microscale information (it would be a tensor function if the microscale had less symmetry). The variable ϕ is the macroscale porosity. They also lead to the continuity equation

$$\boldsymbol{\nabla}\cdot\boldsymbol{u} = A\frac{|\partial\omega_f|}{|\omega|}\frac{\partial R}{\partial t}, \tag{4.19}$$

which indicates that the flow is not incompressible because of the growth of the fibers.

Schematically, the macroscale advection-diffusion-reaction equation for the macroscale concentration C will take the form

$$\frac{\partial C}{\partial t} = \boldsymbol{\nabla}\left(D(\phi)\boldsymbol{\nabla}C - \frac{C}{\phi}(\boldsymbol{U}(\phi) + D(\phi)\boldsymbol{\nabla}\phi)\right) - f(\phi)C. \tag{4.20}$$

The form of the diffusion tensor and reaction term will depend on the details of the homogenization process.

These equations may now be used to describe the macroscopic motion of the interface through the material, and to track the buildup of particles on the fibres comprising the porous structure.

PART TWO

A Macroscopic model

5 Continuum model with evaporation and deposition

We now turn our attention to considering a whole porous medium rather than individual pores. We consider filtration through a planar porous membrane perpendicular to the z-axis, as shown in Figure 13. We assume that the porous medium is saturated with stationary liquid, and that evaporation occurs from the top and bottom of the porous medium. Due to symmetry, we consider only half of the medium, and assume that evaporation happens only from the top interface; we assume no flux of particles at $z = 0$. The porous medium consists of dry and wet (or fluid) regions, Ω_d and Ω_f, respectively. We monitor the particle concentration c as well as porous medium porosity ϕ during the drying process.

The interface between the dry and wet regions is located at $z = h(x,t)$, which we expect to be nontrivial, since we assume that the porous medium porosity $\phi(x,z)$ is non-homogeneous initially and evolves in time (this will be explained in details below). As time evolves, the particle concentration in the wet region changes due to (i) evaporation at $z = h(x,t)$ and (ii) deposition of particles on the porous medium internal structure. We assume there is no effective flow in the wet region, therefore the particle concentration in the wet region follows

$$\frac{\partial(\phi c)}{\partial t} = \boldsymbol{\nabla}\cdot(D\boldsymbol{\nabla}(\phi c)) - f(\phi,c), \quad \text{in} \quad \Omega_f, \tag{5.1}$$

where $c(x,z,t)$ is the concentration of particles per unit volume of fluid in the porous medium, D is the diffusion coefficient of particles in the feed suspension (here assumed constant), and $f(\phi,c)$ is the deposition function, which models how particles carried by the feed are deposited locally within the membrane, and depends on the the local particle concentration and porosity [24, 15, 20, 6, 26]. We apply no flux of particles at the sides of wet region, i.e.

$$\left.\frac{\partial(\phi c)}{\partial x}\right|_{x=0} = \left.\frac{\partial(\phi c)}{\partial x}\right|_{x=L} = \left.\frac{\partial(\phi c)}{\partial z}\right|_{z=0} = 0. \tag{5.2}$$

In addition, at the dry-wet interface, the particles deposition, which only happens due to the particle diffusion, is proportional to the evaporation rate, the particles concentration and the porous media porosity. Therefore, the boundary condition at the dry-wet region interface, where evaporation occurs, is

$$D\boldsymbol{\nabla}(\phi c)\cdot\boldsymbol{n}|_{z=h(x)} = -\lambda E c\phi|_{z=h(x)}\,, \tag{5.3}$$

where λ (dimensionless) is the evaporation coefficient related to the properties of the particles and solvent , $E(\phi,c,h)$ is the evaporation function, and $\boldsymbol{n}$ is the unit normal to the interface which is given by

$$\boldsymbol{n} = \frac{\boldsymbol{\nabla}(z-h(x))}{|\boldsymbol{\nabla}(z-h(x))|}. \tag{5.4}$$

We assume that the membrane porosity decreases as particles are deposited within the

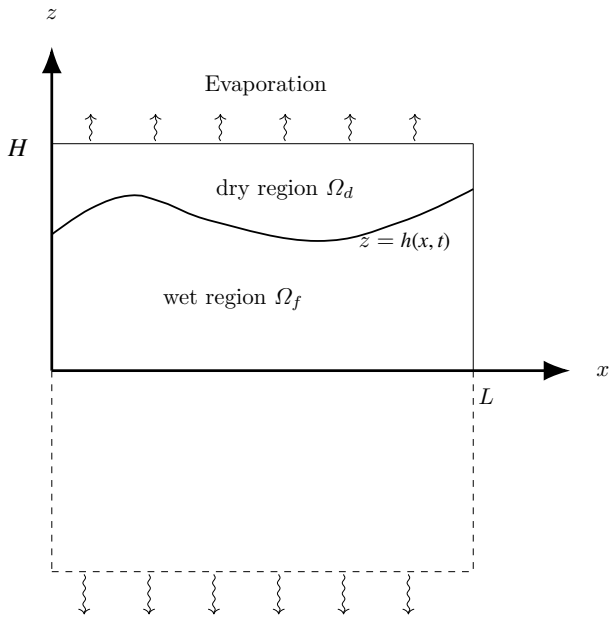

Figure 13. Schematic of a porous medium with length L and thickness H in $x - z$ plane. Evaporation occurs at the top and bottom of the medium. Due to symmetry, only the top half of the porous medium is considered.

internal structure of the porous media, i.e.

$$\frac{\partial \phi}{\partial t} = -f(\phi, c), \tag{5.5}$$

where f is the deposition function and defined as

$$f(\phi, c) = \alpha \phi^{1/2}(c - c^*), \tag{5.6}$$

where α is the average deposition rate of particles relating to the physics of the attraction between particles and pore wall, and c^* represents the saturation concentration of particles. We note that this form of $f(\phi, c)$ allows the particles to detach from the wall and return to solution when c is below the saturation concentration c^*. If we consider a membrane with cylindrical pores of radius r contained within cubes of fixed size, then we can assume the rate of particles arriving at the pore wall should be proportional to pore surface area and the difference between the local particle concentration and the saturation particle concentration [8]. Note that for the proposed membrane structure, the pore surface area scales with $\phi^{1/2}$, since $\phi \sim \left(\frac{r}{\text{cube size}}\right)^2$. Therefore, the adsorption rate is proportional to $\phi^{1/2}(c - c^*)$ and we propose (5.6) for $f(\phi, c)$.

The evolution of the drying front $z = h(x, t)$ is driven by the evaporative flux,

$$\frac{\partial h}{\partial t} = -E(\phi, c, h). \tag{5.7}$$

Evaporation rate of the solvent depends on many factors such as the temperature of the liquid, the pressure difference at the liquid-gas interface, intermolecular forces, and relative humidity in the surrounding air. For example, a commonly-used evaporative

mass flux in evaporating thin film on a uniformly heated substrate takes the form $E = E_0(1+\delta p)/(\mathcal{K}+h)$, where $\mathcal{K}$ measures the thermal resistance to mass transfer at the fluid vapor interface, E_0 characterizes the ratio of the conservative timescale to the non-conservative timescale, and δp describes the influence of the dynamic pressure at the interface that incorporates surface tension and intermolecular forces [5, 19].

In this simplified model, we focus on the influence of particle concentration c and the porosity ϕ to the evaporation, and assumes constant temperature in the liquid and constant relative humidity. The influences of surface tension and intermolecular forces are ignored. Specifically, we consider the following two forms for the evaporative flux, a constant evaporative flux term that assumes spatially-uniform evaporation effects, *i.e.*

$$E = E_0, \tag{5.8}$$

and a non-trivial evaporative sink term that depends on porosity and particle concentration,

$$E(\phi, c) = \frac{E_0 \mathcal{C}_0 \phi}{\mathcal{K}+c}, \tag{5.9}$$

where E_0, $\mathcal{C}_0$ and $\mathcal{K}$ are scaling constants. This form of the evaporative flux originates from the assumption that the solid in the porous media acts as a barrier to local evaporation, and that a higher local particle concentration c leads to lower evaporation effects.

5.1 Nondimensionalization

Next, we nondimensionalize the system using the following scalings,

$$(c, \mathcal{K}) = \mathcal{C}_0(\hat{c}, \hat{\mathcal{K}}), \quad (x, z, h) = L(\hat{x}, \epsilon\hat{z}, \epsilon\hat{h}), \quad t = \frac{1}{\alpha \mathcal{C}_0}\hat{t}, \quad E = E_0\hat{E}, \tag{5.10}$$

where $\epsilon = H/L \ll 1$. For simplicity, we assume the diffusion coefficient D is a constant, while our model can be readily extended to a general scenario. Assuming that the timescale for particle transport diffusion is much shorter than that associated with induced changes to porosity, the resulting system is quasi-static, with time dependence appearing in the porosity evolution and dry-wet interface equations. In other words, we consider the fast diffusion region where equation (5.1) can be reduced to a quasi-static equation [23, 27, 31, 25, 15]. We scale (5.1) to (5.9) using (5.10), dropping $\hat{}$, to obtain

$$\epsilon^2 \frac{\partial^2(\phi c)}{\partial x^2} + \frac{\partial^2(\phi c)}{\partial z^2} = \epsilon^2 w \phi^{1/2}(c - c^*) \quad \text{in } \Omega_f, \quad \text{where} \quad w = \frac{\alpha L^2}{D}, \tag{5.11}$$

$$\left.\frac{\partial(\phi c)}{\partial x}\right|_{x=0} = \left.\frac{\partial(\phi c)}{\partial z}\right|_{x=1} = \left.\frac{\partial(\phi c)}{\partial z}\right|_{z=0} = 0, \tag{5.12}$$

$$\left.\left(-\epsilon^2 \frac{\partial}{\partial x}(\phi c)\frac{\partial h}{\partial x} + \frac{\partial}{\partial z}(\phi c)\right)\right|_{y=h(x)} = -\epsilon^2 \tilde{\lambda} E \phi c|_{z=h(x)}, \quad \text{where} \quad \tilde{\lambda} = \frac{\lambda E_0 L}{D}, \tag{5.13}$$

$$\frac{\mathrm{d}h}{\mathrm{d}t} = -\gamma E, \quad \text{where} \quad \gamma = \frac{E_0}{\epsilon L \alpha \mathcal{C}_0}, \tag{5.14}$$

$$\frac{\partial \phi}{\partial t} = -\phi^{1/2}(c - c^*). \tag{5.15}$$

Note that the unit normal vector is given by

$$\boldsymbol{n} = \frac{\left(-\epsilon\frac{\partial h}{\partial x}, 1\right)}{\sqrt{1+\epsilon^2\left(\frac{\partial h}{\partial x}\right)^2}}.$$

Now we expand all necessary variables in terms of ϵ as

$$i = i_0 + \epsilon^2 i_2 + \mathcal{O}(\epsilon^3), \quad i \in \{h, c, \phi\}. \tag{5.16}$$

Using (5.16) into (5.11)–(5.15), at $\mathcal{O}(1)$, we obtain (considering $\lambda = \mathcal{O}(1)$):

$$\frac{\partial^2(\phi_0 c_0)}{\partial z^2} = 0, \tag{5.17}$$

$$\left.\frac{\partial(\phi_0 c_0)}{\partial x}\right|_{x=0} = \left.\frac{\partial(\phi_0 c_0)}{\partial z}\right|_{x=1} = \left.\frac{\partial(\phi_0 c_0)}{\partial z}\right|_{z=0} = 0, \tag{5.18}$$

$$\frac{\partial(\phi_0 c_0)}{\partial z}|_{z=h(x)} = 0, \tag{5.19}$$

$$\frac{\partial \phi_0}{\partial t} = -\phi_0^{1/2}(c_0 - c^*), \tag{5.20}$$

$$\frac{\mathrm{d}h_0}{\mathrm{d}t} = -\gamma E. \tag{5.21}$$

Using (5.17) in (5.19), we get $\phi_0 c_0 = \beta_0(x)$, $\beta_0'(0) = \beta_0'(1) = 0$. Using (5.16) in (5.11)–(5.15) at $\mathcal{O}(\epsilon^2)$ and setting $\phi c = \beta$ gives

$$\frac{\partial^2 \beta_0}{\partial x^2} + \frac{\partial^2 \beta_2}{\partial z^2} = w\phi_0^{1/2}(c_0 - c^*), \tag{5.22}$$

while the $\mathcal{O}(\epsilon^2)$ version of (5.13) leads to

$$\left[-\frac{\partial \beta_0}{\partial x}\frac{\partial h_0}{\partial x} + \frac{\partial \beta_2}{\partial z}\right]_{z=h_0(x)} = -\tilde{\lambda} E \beta_0|_{z=h_0(x)}. \tag{5.23}$$

Combining (5.22) and (5.23) to obtain

$$-\frac{\partial}{\partial x}\left(h_0\frac{\partial \beta_0}{\partial x}\right) + w\phi_0^{1/2}h_0(c_0 - c^*) = -\tilde{\lambda}E\beta_0, \quad \beta_0'(0) = \beta_0'(1) = 0. \tag{5.24}$$

To summarize, after the nondimensionalization, the leading-order equation for particles is given by (we drop the subscripts for simplicity)

$$-(h(\phi c)_x)_x + whf(\phi, c) + \tilde{\lambda}E\phi c = 0, \tag{5.25a}$$

where $f(\phi, c) = \phi^{1/2}(c_0 - c^*)$. The evolution of the dry-wet interface $z = h(x, t)$ due to evaporation is governed by

$$\frac{\partial h}{\partial t} = -\gamma E(\phi, c), \quad E \equiv 1 \quad \text{or} \quad E(\phi, c) = \frac{\phi}{\hat{\mathcal{K}} + c}. \tag{5.25b}$$

Finally, the model for the porosity ϕ due to particle deposition reduces to

$$\frac{\partial \phi}{\partial t} = -f(\phi, c), \quad f(\phi, c) = \phi^{1/2}(c - c^*). \tag{5.25c}$$

5.2 Numerical simulations

We numerically simulate the leading-order PDE system (5.25) to investigate the behavior of the solutions. Since the system contains a second-order ODE (5.25a) that characterizes the quasi-static relation among ϕ, c, and h, and two time-dependent differential equations (5.25b) and (5.25c), we solve the system iteratively. Given fixed initial conditions (5.26) on the dry-wet interface height h and the porosity ϕ,

$$h(x,0) = \tilde{h}_0 \equiv 1, \quad \phi(x,0) = \tilde{\phi}_0(x) = 0.3(1 + 0.5\cos(\pi x)), \tag{5.26}$$

we first solve the second-order ODE (5.25a) for the particle concentration c over $0 \le x \le 1$ subject to no-flux boundary conditions

$$\frac{\partial c}{\partial x} = 0 \quad \text{at} \quad x = 0, 1. \tag{5.27}$$

Then the evaporative flux $E(\phi, c)$ and the deposition function $f(\phi, c)$ on the right-hand-side of equations (5.25b) and (5.25c) are updated based on the obtained profile of the particle concentration c. The differential equations (5.25b) and (5.25c) are then used to obtain the porosity ϕ as well as the dry-wet interface h at a new time step, which will be used to solve (5.25a) again for the updated particle concentration c at the new time step. Finite differences are used to solve the quasi-static equation (5.25a) and we apply the forward Euler method for the time stepping of equations (5.25b) and (5.25c) in MATLAB.

To capture the overall evolution of the dry-wet interface, it is useful to define an effective evaporation rate based on the averaged evaporative flux over the domain,

$$\bar{E} = \int_0^1 E(\phi, c)\, dx. \tag{5.28}$$

For all the simulations presented in this section, we set the dimensionless parameters $\tilde{\lambda} = 1$, $c^* = 0.1$, $\hat{\mathcal{K}} = 1$, and $w = 1$. We will focus on the influence of the form of the evaporative flux E on the system.

In Figure 14, we present the dynamic evolution of the film thickness h, particle concentration c, and porosity ϕ in time with $\gamma = 0.1$. Correspondingly, the effective evaporation rate $\bar{E} = 0.1$ holds for all time. While the film thickness h decreases uniformly in time due to the constant evaporative flux, the initial spatial variation in the porosity ϕ_0 increases in time. We also observe that regions with higher porosity have lower particle concentration, and as the porosity ϕ approaches zero near $x = 1$, the particle concentration profile c develops a peak. This is consistent with physical intuition as particles are trapped in smaller pore spaces as the local porosity approaches zero.

In Figure 15, we show a simulation when the evaporative flux takes the form $E(\phi, c) = \phi/(\hat{\mathcal{K}} + c)$. Since the evaporative flux is proportional to the porosity ϕ, the film thickness h decreases at a faster rate in regions where the porosity ϕ is high. The dynamics of the particle concentration and the porosity is similar to those in the constant evaporative flux case. The effective evaporation rate $\bar{E}$ increases in time as the particle concentration c and the porosity ϕ vary during the evaporation.

The preliminary numerical results in Figures. 14 and 15 show that the solution of the leading-order model (5.25) is sensitive to the form of the evaporative flux and the diffusion effects. Further studies on this model may focus on the solution structure of the

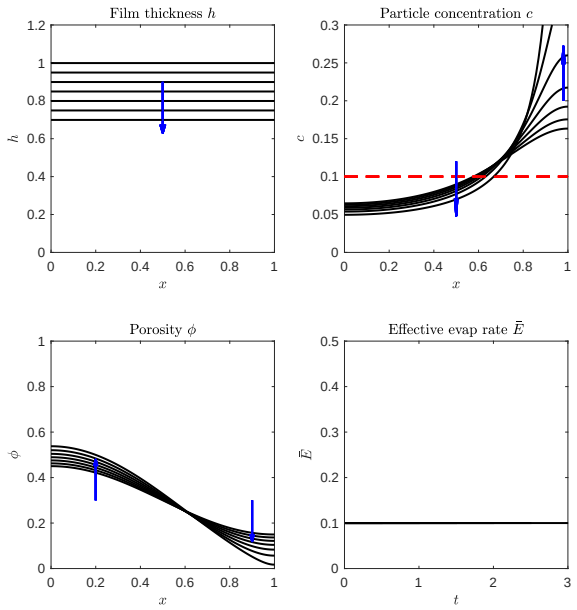

Figure 14. Numerical simulation of (5.25) with the initial and boundary conditions specified by equations (5.26) and (5.27). Other system parameters are $\tilde{\lambda} = 1$, $c^* = 0.1$, $w = 1$, and $\gamma = 0.1$.

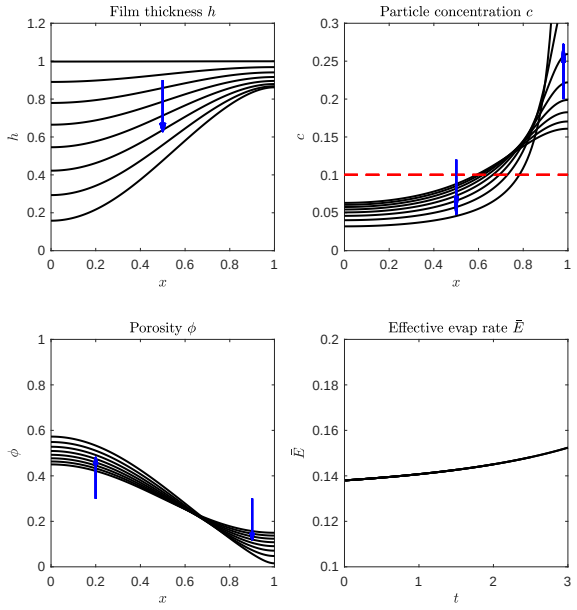

Figure 15. Numerical simulation of (5.25) with the evaporative flux $E(\phi, c) = \phi/(\hat{\mathcal{K}} + c)$ where $\hat{\mathcal{K}} = 1$. Other system parameters are $\tilde{\lambda} = 1$, $c^* = 0.1$, $w = 1$, and $\gamma = 0.5$.

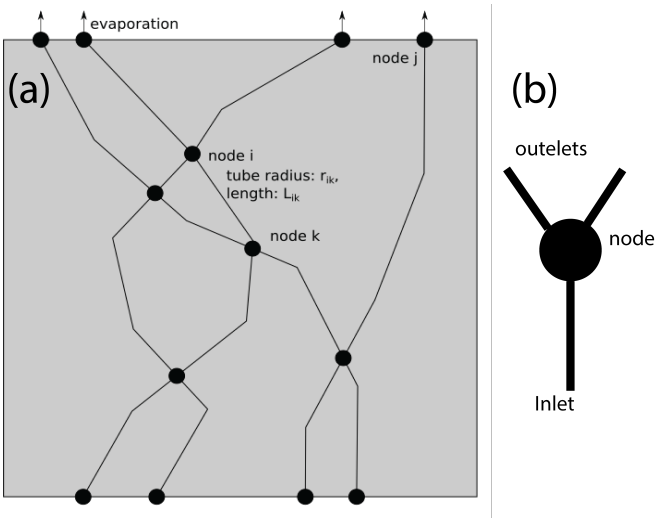

Figure 16. a) A schematic of mapping the membrane to a network of connected edges assuming evaporation happens from the top. b) Single node example used in the simulation.

quasi-static ODE (5.25a) and its dependence on the modeling of the evaporative flux E. It would also be interesting to investigate the influence of the initial film thickness and porosity profile on the later stage dynamics and the estimate of the effective evaporation rate $\bar{E}$.

6 Network Approach to Examine Macroscopic Capillary Effects

6.1 Introduction

The goal of a network model is to use the physics of evaporation at the scale of a single pore and solve the problem of evaporation in a large membrane through conservation at the nodes in the system. This approach simplifies the problem compared to an attempt to solve evaporation across multiple connected pores while it preserves the physics of evaporation in a single pore. Network models have been successfully applied to various problems in flow in porous media, including single-phase flow across a two-dimensional network [2], and filtration in membranes [10]. Additionally, network models have been validated by comparing their results with experimental measurements and show a very good agreement with pore-level velocity measurements[2].

6.2 Model formulation

The network model is based on mapping the complex network onto a graph with edges and nodes. The edges are a realistic map of the membrane percolating path. The nodes map to the pores of the network where multiple edges meet or branch from, as shown in Figure 16 a. The flux is distributed between the edges at each node. Connectivity is essential in this mapping and dead-end areas do not appear as part of the final graph.

To determine the flow in the medium, we determine the dynamics in each edge knowing the pressure gradient along the edge between nodes i and j, $\Delta P = P_i - P_j$, and the conductance of the edge, k_{ij}. Since the liquid velocity is slow in most porous media flow, the flux, Q_{ij}, in each edge can be described using the Hagen-Poiseuille equation

$$Q_{ij} = k_{ij}(P_i - P_j), \tag{6.1}$$

where k_{ij} depends on the physical properties of the edge and the viscosity of the fluid, μ; for example, assuming that the edges are tubes with radius R_{ij} and length L_{ij},

$$k_{ij} = \frac{\pi R_{ij}^4}{8\mu L_{ij}}. \tag{6.2}$$

We assume the network is initially connected. However, once an edge becomes blocked with particles, we assume that it does not connect two nodes anymore and we set the conductance of that edge is zero. To drive the flow across a medium, fluid has to pass from edges to nodes and nodes to other edges in this connected network. The flux across the network at each instant is determined by the conservation of flux at each node:

$$\sum_{i,j} Q_{ij} = 0. \tag{6.3}$$

This means that the incoming flux to a node should be distributed between the outgoing edges. The distribution of fluxes depends on the conductance of the connected edges.

6.3 Results

To develop and test the network model, we first solve for the conservation of flux in a network with a few edges and one node as seen in Figure 16b. Here, we choose an arbitrary conductance for each edge and apply pressure on the inlet and outlet of the network and solve for flux in each edge. Although the preliminary results are satisfying, we anticipate that a more efficient method needs to be applied to a large network with a considerable number of nodes. Gu *et al.* [9] introduce an incident matrix representation that can be used to solve for flux and pressure in large networks efficiently. The incident matrix is a linear operator similar to (6.1). Once the network is mapped to a graph, the matrix of conductance is calculated, and by knowing the pressure on the sides of the network, we solve for the flux. The pressure matrix is updated at each step if there are any changes in any physical parameters in the network. This change can be due to clogging, retention of materials, or dissolution of the solid matrix on an edge. Interestingly, we do not need to incorporate the physics of the phenomena happening in the porous medium and solve for the dynamics except for updating the conductance matrix in each iteration.

To the best of our knowledge, incorporating evaporation into a network model has not yet been done. In most problems, external pressure or flow rate is applied across the network and fluids are constantly present across the entire network. This allows for solving the problem without necessarily incorporating the role of dynamics at the pore level. However, evaporation inside a porous medium is fundamentally a different problem since no external pressure is applied. The occupancy of an edge at any time is determined by *i*) its exposure to the air-water interface and *ii*) the rate of evaporation within the

edge. This means if an edge is not exposed to air, it is occupied but if the edge is exposed to air, we consider evaporation. Within an edge that evaporation happens, a pore-level model of evaporation will be applied as in §3. To apply the network model, we update the pressure, P_{ij} depending on the rate of evaporation in each edge and occupancy of an edge with water. The conductance, k_{ij}, of the edges, needs to be updated regularly since edges that carry no fluid do not contribute to flux or pressure gradient, and $k_{ij} = 0$ if the edge is dry.

As mentioned above, to fully implement the network model to evaporation and drying of a porous medium, the presence, or not, of liquid in an edge dictates how the pressure across the medium is updated. The choice of an appropriate pore-level model that captures the relative time-scale for evaporation in individual pores across the medium and the rate for updating the changes in pressure in each pore is crucially important. A poor choice can lead to an unrealistically saturated medium.

7 Conclusions and discussion

In this report, we have considered the drying out of a filter saturated with liquid containing contaminant particles. In §2, we focused on a reduced model for contaminant transport and deposition from a volatile liquid solution in a single axisymmetric pore. The simple and efficient numerical simulations for this model make it possible to explore the influences of different system parameters on the distribution of deposited particles along the pore walls. These simulations could be used to inform larger-scale homogenization or network models. In a single pore, for initially under-saturated solutions, we found that deposition is slower and involves less material than in an over-saturated liquid, which yield a gradient in the pore radius immediately from the inlet. For dilute solutions, the model suggests that clogging typically occurs in the middle of the pore, but more study may be needed using models that remain valid for high concentrations or incorporate more complicated evaporation rates. Numerical simulations of the model also show that cumulative deposition from repeated wetting/drying cycles can resemble profiles in pores with initially tapered geometries.

In §3, we built and solved a very simple model for a long and thin droplet of liquid moving in a converging 2-D pore under the influence of surface tension and evaporation. We neglected particle transport. We reduced the model to a pair of ODEs for the ends of the droplet, which we solved numerically. We observed that there was an interesting interplay between capillary forces, which promoted motion towards the diverging end of the pore when the liquid was pore-surface-ophobic, and evaporation, which caused each air-liquid interface to move towards the centre of the droplet.

In §4, we sketched the framework for systematically averaging the precipitation of particles onto the microscale porous structure and coupling this with the macroscopic motion of the evaporating interface.

In §5, we presented a simple mathematical model to describe the key elements of evaporation in porous media, which includes an advection-diffusion equation for the particle transport and deposition of particles within the porous membrane as well as variations in the membrane porosity due to particle deposition and evaporation. Assuming that the timescale for particle transport diffusion is much shorter than that associated with

induced changes to porosity, the resulting system is quasi-static, with time dependence appearing in the porosity evolution and dry-wet interface equations. Given the complexity of the membrane structure, the chemical interactions between the filtrate particles and the membrane material, and the evaporation conditions (which may vary from one application to another), our simplified model necessarily contains several parameters that could be difficult to measure for a particular membrane-evaporation system. Our model is able to describe how the dry-wet interface evolves across the porous medium, and predicts how particles are deposited within the porous medium and change the membrane porosity. Our results show that the dry-wet interface and the membrane porosity evolution are sensitive to the form of the evaporative flux and the particle diffusion. In addition, we found out that regions with higher porosity have lower particle concentration, and as the porosity approaches zero, the particle concentration profile develops a peak.

The use of a simplified network model (explained in §6) provides a viable alternative to a full numerical solution of the dynamics of two-phase flow in evaporation. We demonstrated that this method helps reduce a complicated network of connected pores to a matrix representation of the basic physical properties of edges. Additionally, we expect that this method can be used to examine models of evaporation in single pores. By comparing the rate of evaporation and clogging from a network model with experimental results, the rate of evaporation in a single pore will be quantified.

Our work during the study group, as presented in this report, ties together multiple different approaches to modelling evaporation and deposition in filters and provides Gore with some key avenues for future exploration.

References

[1] M Aboufoul, Nima Shokri, Ehab Saleh, C Tuck, and Alejandro Garcia. Dynamics of water evaporation from porous asphalt. *Construction and Building Materials*, 202:406–414, 2019.

[2] K. Alim, S. Parsa, D. A. Weitz, and M. P. Brenner. Local pore size correlations determine flow distributions in porous media. *Phys. Rev. Lett.*, 119:144501, Oct 2017.

[3] R. Byron Bird, Warren E. Stewart, and Edwin N. Lightfoot. *Transport Phenomena, Revised 2nd Edition*. John Wiley & Sons, Inc., hardcover edition, 12 2006.

[4] C. Breward, F. Brosa Planella, D A. Edwards, K. Kiradjiev, A. Kovacs, S. G. Llewellyn Smith, D. Rumschitzki, P. Sanaei, Y. Sun, T. Witelski, and M. Zyskin. Evaporation from porous media, pore-level analysis. 36th MPI Workshop report https://mpi2020.w3.uvm.edu/finalReports/FinalReport_Gore_2020.pdf, University of Vermont, 2020.

[5] J. P. Burelbach, S. G. Bankoff, and S. H. Davis. Nonlinear stability of evaporating/condensing liquid films. *Journal of Fluid Mechanics*, 195:463–494, 1988.

[6] Zhengyi Chen, Shi Yue Liu, Ivan C Christov, and Pejman Sanaei. Flow and fouling in elastic membrane filters with hierarchical branching pore morphology. *Physics of Fluids*, 33(6):062009, 2021.

[7] M. Dalwadi, M. Bruna, and I. M. Griffiths. Homogenisation problems in reactive decontamination. *J. Fluid Mech.*, 809:264–289, 2016.

[8] D Fong, LJ Cummings, SJ Chapman, and P Sanaei. On the performance of multilayered membrane filters. *Journal of Engineering Mathematics*, 127(1):1–25, 2021.

[9] B. Gu, L. Kondic, and L. J. Cummings. A graphical representation of membrane filtration. *arXiv:2106.03915 [physics.flu-dyn]*, 2021.

[10] B. Gu, D. L. Renaud, P. Sanaei, L. Kondic, and L. J. Cummings. On the influence of pore connectivity on performance of membrane filters. *Journal of Fluid Mechanics*, 902:A5, 2020.

[11] Wolfram Research, Inc. Mathematica, Version 12.3.1. Champaign, IL, 2021.

[12] C. N. Kaplan and L. Mahadevan. Evaporation-driven ring and film deposition from colloidal droplets. *Journal of Fluid Mechanics*, 781, 2015.

[13] V. G. Kevich and V. S. Krylov. Surface-tension-driven phenomena. *Annu. Rev. Fluid Mech.*, 1:293–316, 1969.

[14] Peter Lehmann, Shmuel Assouline, and Dani Or. Characteristic lengths affecting evaporative drying of porous media. *Physical Review E*, 77(5):056309, 2008.

[15] Shi Yue Liu, Zhengyi Chen, and Pejman Sanaei. Effects of particles diffusion on membrane filters performance. *Fluids*, 5(3):121, 2020.

[16] E. Luckins, C. J. W. Breward, I. M. Griffiths, and Z. Willmott. Homogenisation problems in reactive decontamination. *Euro. J. Appl. Math.*, 31:782–805, 2019.

[17] Thomas Metzger and Evangelos Tsotsas. Influence of pore size distribution on drying kinetics: A simple capillary model. *Drying Technology*, 23(9-11):1797–1809, 2005.

[18] Charles Monroe and John Newman. The effect of interfacial deformation on electrodeposition kinetics. *Journal of The Electrochemical Society*, 151(6):A880, 2004.

[19] A. Oron, S. H. Davis, and S. G. Bankoff. Long-scale evolution of thin liquid films. *Rev. Mod. Phys.*, 69:931–980, 1997.

[20] Dave Persaud, Mikhail Smirnov, Daniel Fong, and Pejman Sanaei. Modeling of the effects of pleat packing density and cartridge geometry on the performance of pleated membrane filters. *Fluids*, 6(6):209, 2021.

[21] J. R. Philip. Evaporation, and moisture and heat fields in the soil. *Journal of Atmospheric Sciences*, 14(4):354–366, 1957.

[22] A. F. Routh and W. B. Zimmerman. Distribution of particles during solvent evaporation from films. *Chemical Engineering Science*, 59(14):2961–2968, 2004.

[23] Pejman Sanaei. Mathematical modeling of membrane filtration. 2017.

[24] Pejman Sanaei and Linda J Cummings. Flow and fouling in membrane filters: effects of membrane morphology. *Journal of Fluid Mechanics*, 818:744–771, 2017.

[25] Pejman Sanaei and Linda J Cummings. Membrane filtration with complex branching pore morphology. *Physical Review Fluids*, 3(9):094305, 2018.

[26] Pejman Sanaei and Linda J Cummings. Membrane filtration with multiple fouling mechanisms. *Physical Review Fluids*, 4(12):124301, 2019.

[27] Pejman Sanaei, GW Richardson, T Witelski, and LJ Cummings. Flow and fouling in a pleated membrane filter. *Journal of Fluid Mechanics*, 795:36–59, 2016.

[28] N Shokri, Peter Lehmann, and Dani Or. Effects of hydrophobic layers on evapo-

ration from porous media. *Geophysical Research Letters*, 35(19), 2008.

[29] Salomé MS Shokri-Kuehni, Thomas Vetter, Colin Webb, and Nima Shokri. New insights into saline water evaporation from porous media: Complex interaction between evaporation rates, precipitation, and surface temperature. *Geophysical Research Letters*, 44(11):5504–5510, 2017.

[30] J. M. Stewart and P. Broadbridge. Calculation of humidity during evaporation from soil. *Advances in water resources*, 22(5):495–505, 1999.

[31] Yixuan Sun, Pejman Sanaei, Lou Kondic, and Linda J Cummings. Modeling and design optimization for pleated membrane filters. *Physical Review Fluids*, 5(4):044306, 2020.

[32] Jaap Van Brakel. Mass transfer in convective drying. 1980.

[33] S. Whitaker. Simultaneous heat, mass, and momentum transfer in porous media: a theory of drying. In *Advances in heat transfer*, volume 13, pages 119–203. Elsevier, 1977.